



GALACTIC COSMIC RAYS IN THE LOCAL INTERSTELLAR MEDIUM: VOYAGER 1 OBSERVATIONS AND MODEL RESULTS

A. C. CUMMINGS¹, E. C. STONE¹, B. C. HEIKKILA², N. LAL², W. R. WEBBER³, G. JÓHANNESSEN⁴,

I. V. MOSKALENKO⁵, E. ORLANDO⁵, AND T. A. PORTER⁵

¹California Institute of Technology, Pasadena, CA 91125, USA

²Goddard Space Flight Center, Greenbelt, MD 20771, USA

³New Mexico State University, Las Cruces, NM 88003, USA

⁴University of Iceland, Reykjavik, Iceland

⁵HEPL and KIPAC, Stanford University, Stanford, CA 94305, USA

Received 2016 March 29; revised 2016 April 21; accepted 2016 April 22; published 2016 October 21

ABSTRACT

Since 2012 August *Voyager 1* has been observing the local interstellar energy spectra of Galactic cosmic-ray nuclei down to 3 MeV nuc⁻¹ and electrons down to 2.7 MeV. The H and He spectra have the same energy dependence between 3 and 346 MeV nuc⁻¹, with a broad maximum in the 10–50 MeV nuc⁻¹ range and a H/He ratio of 12.2 ± 0.9 . The peak H intensity is ~ 15 times that observed at 1 AU, and the observed local interstellar gradient of 3–346 MeV H is $-0.009 \pm 0.055\% \text{AU}^{-1}$, consistent with models having no local interstellar gradient. The energy spectrum of electrons ($e^- + e^+$) with 2.7–74 MeV is consistent with $E^{-1.30 \pm 0.05}$ and exceeds the H intensity at energies below ~ 50 MeV. Propagation model fits to the observed spectra indicate that the energy density of cosmic-ray nuclei with > 3 MeV nuc⁻¹ and electrons with > 3 MeV is $0.83\text{--}1.02 \text{eV cm}^{-3}$ and the ionization rate of atomic H is in the range of $1.51\text{--}1.64 \times 10^{-17} \text{s}^{-1}$. This rate is a factor > 10 lower than the ionization rate in diffuse interstellar clouds, suggesting significant spatial inhomogeneity in low-energy cosmic rays or the presence of a suprathermal tail on the energy spectrum at much lower energies. The propagation model fits also provide improved estimates of the elemental abundances in the source of Galactic cosmic rays.

Key words: cosmic rays – ISM: abundances – ISM: clouds

Supporting material: machine-readable tables

1. INTRODUCTION

On 2012 August 25 (2012/238), *Voyager 1* (*VI*) entered a region of space in which the heliospheric ions and electrons were depleted and the Galactic cosmic-ray (GCR) intensity was enhanced (Krimigis et al. 2013; Stone et al. 2013). Although the location of *VI* relative to the heliopause is still being debated (Gurnett et al. 2013; Gloeckler & Fisk 2014; Fisk & Gloeckler 2014), it is generally agreed that *VI* has been observing low-energy GCRs from the local interstellar medium (LISM) since that time (Krimigis et al. 2013; Stone et al. 2013; Gloeckler & Fisk 2014). For the following discussion, we will assume that *VI* did cross the heliopause on 2012 August 25, but the results will not depend on that assumption.

In Figure 1 we show the PENH counting rate of GCRs from the HET 2 (High Energy Telescope 2) on the *VI* Cosmic Ray Subsystem (CRS) instrument (Stone et al. 1977) from day 251 of 1977 to day 280 of 2015 (1977/251–2015/280). The PENH rate is due to GCR nuclei and electrons that trigger the thresholds of the first two detectors of the B-end of HET (*B1* and *B2*) and the threshold of the *C1* detector, which is the last detector in the B-end stack of detectors. It is an integral counting rate of GCR nuclei with energy $\gtrsim 70$ MeV nuc⁻¹ and of electrons $\gtrsim 15$ MeV. (See Section 5).

The crossing of the heliopause is marked in the figure. Figure 2 of Stone et al. (2013) showed that residual heliospheric particles persisted into the interstellar medium (ISM) for about 100 days after the heliopause crossing. Only small, transient fluctuations due to passing disturbances from the Sun (Gurnett et al. 2015) are observed after that. Accordingly, for most nuclei with $1 \leq Z \leq 28$ and for electrons, we have

selected the period 2012/342 through 2015/181 for most of the analysis in this paper.

We also show new models of interstellar spectra that are partly constrained by these new observations. The models are used to estimate the energy density of cosmic rays in the LISM and the cosmic-ray ionization rate of atomic H at cosmic-ray energies above 3 MeV nuc⁻¹. This part of the work represents an update to a study published in 1998 (Webber 1998) before there were direct observations of the energy spectra at low energies in the LISM. See also Cummings et al. (2015) for a preliminary version of this work. For a recent review of Galactic cosmic rays see Grenier et al. (2015).

In this paper, all *Voyager* measurements will either be of electrons ($e^- + e^+$) or of elements; no isotope energy spectra will be presented. The data selections for H, for example, will include protons and deuterium. Deuterium is a very small contributor to the H energy spectrum, so in many cases the term protons will be used when referring to the element H. Similarly, the observed He energy spectra will contain both ³He and ⁴He.

2. GRADIENTS

In Figure 2 we show the intensity in four energy bands of protons from the *VI* CRS instrument plotted versus distance in AU for the time period 2012/342–2015/181. As was reported in Krimigis et al. (2013), a small anisotropy of GCRs exists in the LISM with the property that the intensity of > 211 MeV protons is often reduced in the two 45° wide sectors of the Low-Energy Charged Particle (LECP) instrument that are approximately centered on the perpendicular to the interstellar magnetic field. The magnitude of the intensity reduction varies with time over timescales of months but is typically $< 10\%$.

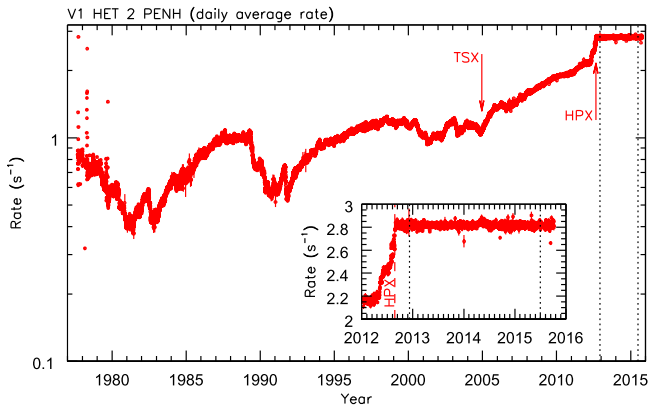


Figure 1. PENH counting rate dominated by protons >70 MeV from 1977/251 through 2015/280 from the *V1* CRS instrument. The crossing of the solar wind termination shock is labeled by TSX and that of the heliopause by HPX. The inset shows the time period since 2012.0 in more detail. The vertical dotted lines show the boundaries of the time period selected for most of the analysis.

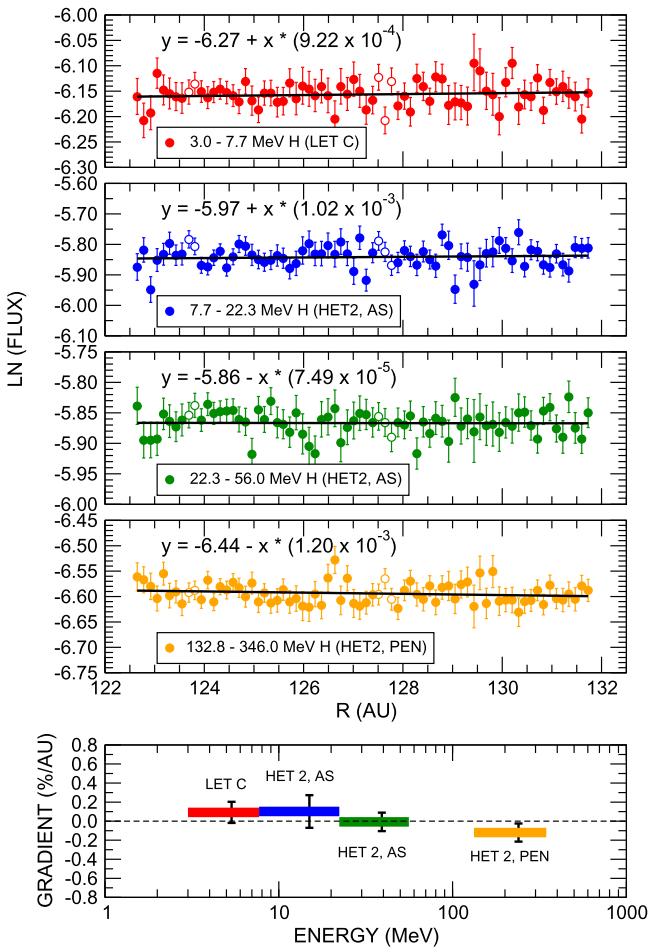


Figure 2. Top four panels: intensity of protons in four energy bands vs. heliocentric radial distance of *V1*. The open symbols in the top four panels represent data acquired during transient disturbances and were not included in the fits. The time period covered is 2012/342–2015/181. All data are plotted with statistical uncertainties only. The equations representing the fits are shown in the panels with y being the ordinate and x being the abscissa. Bottom panel: radial gradient vs. energy. The labels refer to data from different telescopes and modes, which are described in the Appendix (see also Stone et al. 1977).

The data shown in Figure 2 come from CRS telescopes whose nominal fields of view do not overlap with those of the affected sectors from LECP.

Table 1
Radial Gradients of Protons from *V1* for the Period 2012/342–2015/181

Energy Range, MeV	Gradient, % AU ⁻¹
3.0–7.7	0.09 ± 0.11
7.7–22.3	0.10 ± 0.17
22.3–56.0	-0.01 ± 0.10
133–346	-0.12 ± 0.10

In Figure 2, we have also excluded data from periods when CRS was pointing in off-nominal directions. There are two off-nominal pointing situations that can occur on *V1*: (1) rolls about the axis pointed toward Earth, which are executed to calibrate the magnetometer, and (2) a reorientation of the spacecraft about the same axis by 70° to allow LECP to scan in a different scan plane. The percentage of accumulation time removed from the period 2012/342–2015/181 for these two situations was 1.1% for (1) and 3.4% for (2).

Further, we have removed data during two periods when intensity enhancements due to passing disturbances were observed. These events have been discussed in Gurnett et al. (2015) and occurred near day 80 of 2013 and near day 110 of 2014. The days of data removed were 2013/78–103 and 2014/104–142. The percentage of accumulation time removed for these events from the period 2012/342–2015/181 was 7.1%. By excluding these data, the most accurate estimates of the true radial gradients are obtained.

Fits to a linear function of the data are shown in Figure 2, with the coefficient of the distance parameter times 100 representing the radial gradient in % AU⁻¹. The gradients and uncertainties in the four energy intervals are shown in the bottom panel of Figure 2 and are tabulated in Table 1. Over this period the radial gradient is consistent with zero with the weighted average equal to $-0.009 \pm 0.055\%$ AU⁻¹ over the energy range 3–346 MeV.

3. ENERGY SPECTRA, ELEMENTS

For the construction of the *V1* energy spectra we did not exclude any time periods for off-nominal pointing or for the two transient events. In addition, we added data from LET D (Low Energy Telescope D) to the energy spectra analysis to improve statistics. To check if these changes would bias the energy spectra, we constructed the energy spectrum of H in the two different ways for the energy interval 3–56 MeV and found that the biggest intensity difference in any energy interval was 2%, well below our estimate of systematic uncertainty.

In Figure 3 we show the elemental H and He energy spectra from the *V1* CRS instrument for the period 2012/342–2015/181, as well as energy spectra from other missions at 1 AU during a solar minimum time period. The *V1* energy spectra of both H and He have a broad peak in the 10–50 MeV nuc⁻¹ energy range. The rollover of the energy spectra at low energies from a power law at high energies is likely a consequence primarily of ionization energy losses (Ip & Axford 1985) and suggests that *V1* is not in the nearby vicinity of a recent source of GCRs.

The effects of solar modulation are evident when comparing the peak intensities and the energies of the peak intensities of the *V1* H and He energy spectra with those of the 1 AU energy spectra. The 1 AU energy spectra have lower peak intensities and peak at higher energies than do the newly measured *V1* LISM energy spectra. For example, the peak intensity of the *V1*

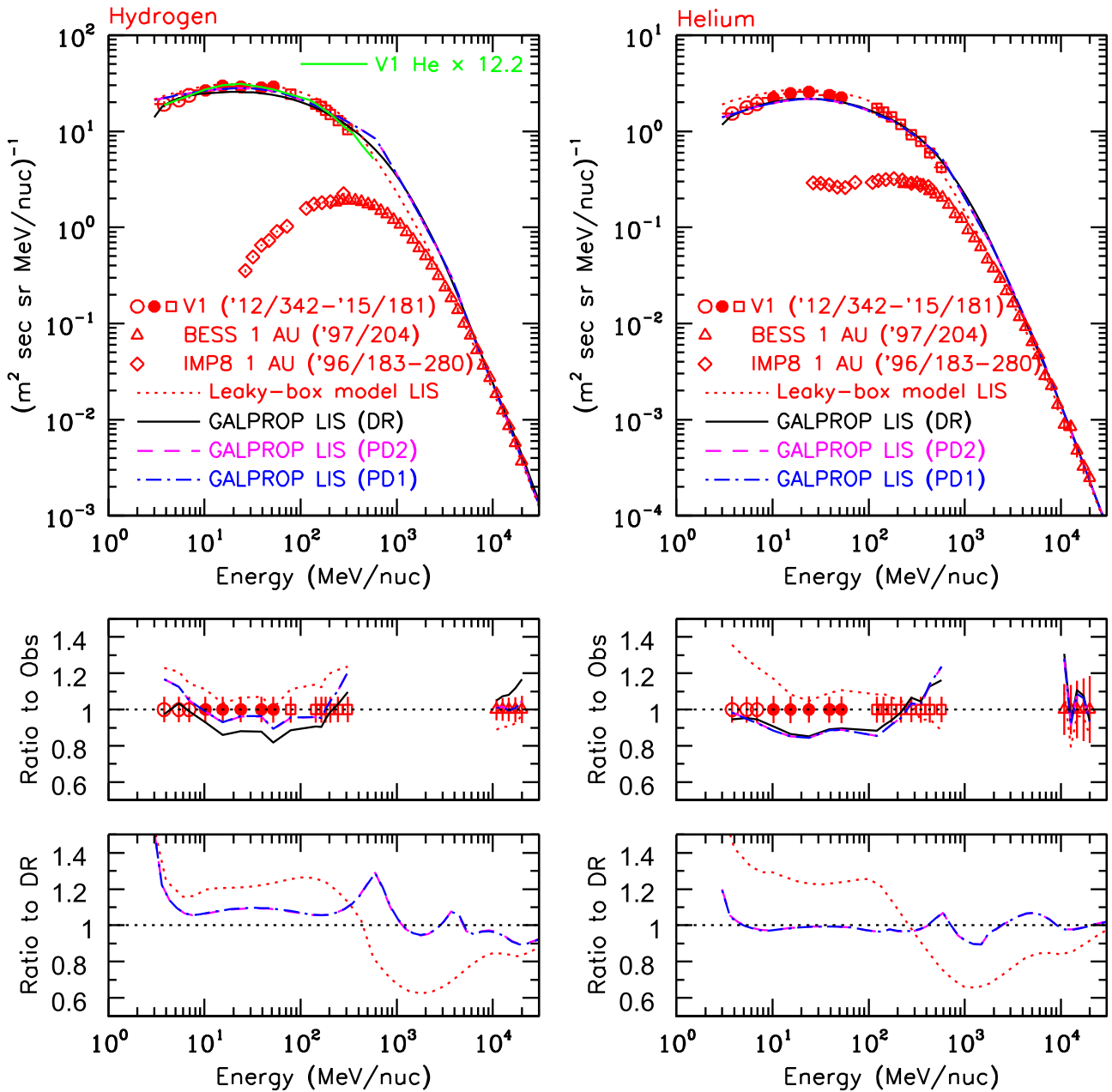


Figure 3. Top row: differential energy spectra of H (left) and He (right) from V1 for the period 2012/342–2015/181, and solar-modulated spectra at 1 AU from a BESS balloon flight in 1997 (Shikaze et al. 2007) and from IMP8 in the latter part of 1996 (McDonald 1998). The three different symbols for the V1 data correspond to different telescope types described in the Appendix. All data are plotted with their statistical and systematic uncertainties added in quadrature. Also shown are estimated spectra in the LISM from a leaky-box model and three GALPROP models as described in the text. Middle row: ratio of model intensities to V1 observations below $\sim 600 \text{ MeV nuc}^{-1}$ and to BESS observations above $\sim 10 \text{ GeV nuc}^{-1}$. Bottom row: ratio of models to GALPROP DR model. Note that for H and He, the GALPROP PD1 and PD2 models are essentially identical. Data analysis techniques used to derive the *Voyager* data are described in the Appendix and the *Voyager* data are listed in Tables 7 and 8.

H energy spectrum is ~ 15 times that of the peak intensity of H at 1 AU.

The V1 GCR H/He ratios in the LISM in three energy intervals are shown in Table 2. The ratio is essentially energy independent from $3\text{--}346 \text{ MeV nuc}^{-1}$ (see green line in left panel of the Figure 3) with an average value of 12.2 ± 0.9 . We note that such an energy-independent ratio would not be expected in the energy region of the peak intensities if the particles were being subjected to rigidity-dependent solar modulation.

Table 2
Ratios of GCR H to He from V1 for the Period 2012/342–2015/181

Energy Range, MeV	H/He ratio
3.0–7.7	12.2 ± 0.9
7.7–56	12.0 ± 0.9
134–346	12.3 ± 0.9

Note. Uncertainties are statistical and 5% point-to-point systematic added in quadrature.

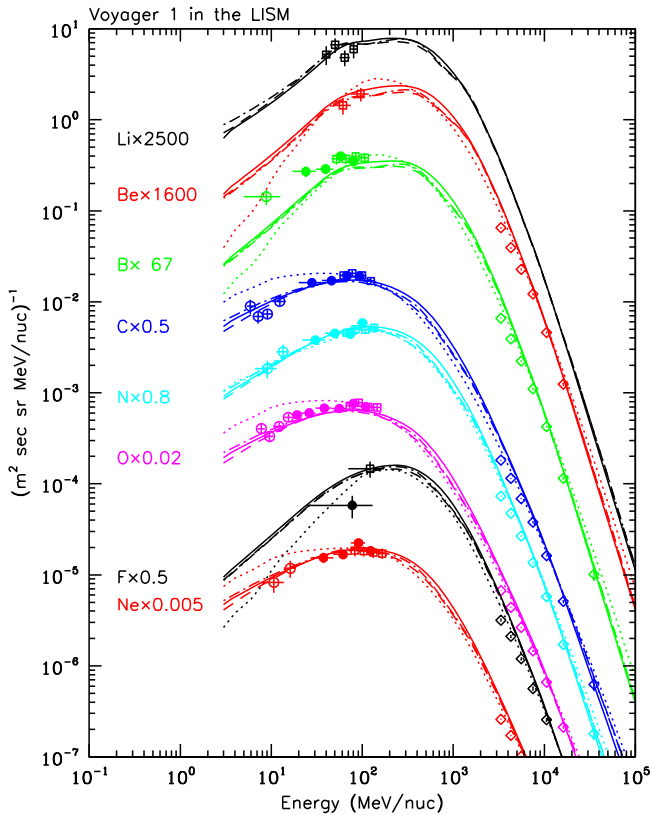


Figure 4. Differential energy spectra from *V1*. The different symbols for the *V1* data correspond to different telescope types described in the Appendix. The data are plotted with the statistical and systematic uncertainties added in quadrature. At energies above ~ 3 GeV nuc $^{-1}$ the data are from the HEAO-3-C2 instrument (Engelmann et al. 1990). Also shown are estimated spectra in the LISM from a leaky-box model and three GALPROP models as described in the text. The line types for the models are the same as in Figure 3 and are as follows: dotted for LBM, solid for GALPROP DR, dashed for GALPROP PD2, and dot-dashed for GALPROP PD1. The time period for the open and closed circles is 2012/342–2015/181; the time period for the open squares is 2012/342–2014/365. The *Voyager* data are listed in Table 9.

The estimated interstellar energy spectra from a leaky-box model (LBM) and three GALPROP models are also shown. The GALPROP models are labeled DR for diffusive reacceleration and PD1 and PD2 for plain diffusion with one or two breaks in the injection spectrum for $Z > 2$ nuclei, respectively. Both the LBM and the GALPROP models are described in more detail in the Appendix.

Also shown in Figure 3 are panels displaying ratios of the model intensities to a subset of the observations. The model intensities bracket the observations with the deviations being typically $\lesssim \pm 20\%$. In the bottom set of panels of Figure 3 we show the ratios of three of the models to the GALPROP DR model. Again there are significant differences and at energies above ~ 1 GeV nuc $^{-1}$ these differences will prove to be important for calculating the energy density of GCRs. Thus our calculations of energy density and ionization rate, which will be based on the model spectra, will give a range of values that will represent a systematic uncertainty in our results.

Figure 4 shows energy spectra from the CRS instrument on *V1* of eight nuclei from Li through Ne, along with calculated intensities from the four models for the LISM. We also show the energy spectra at 1 AU from the HEAO-3-C2 instrument (Engelmann et al. 1990) above 3 GeV nuc $^{-1}$ where the effects of solar modulation should be significantly reduced. The

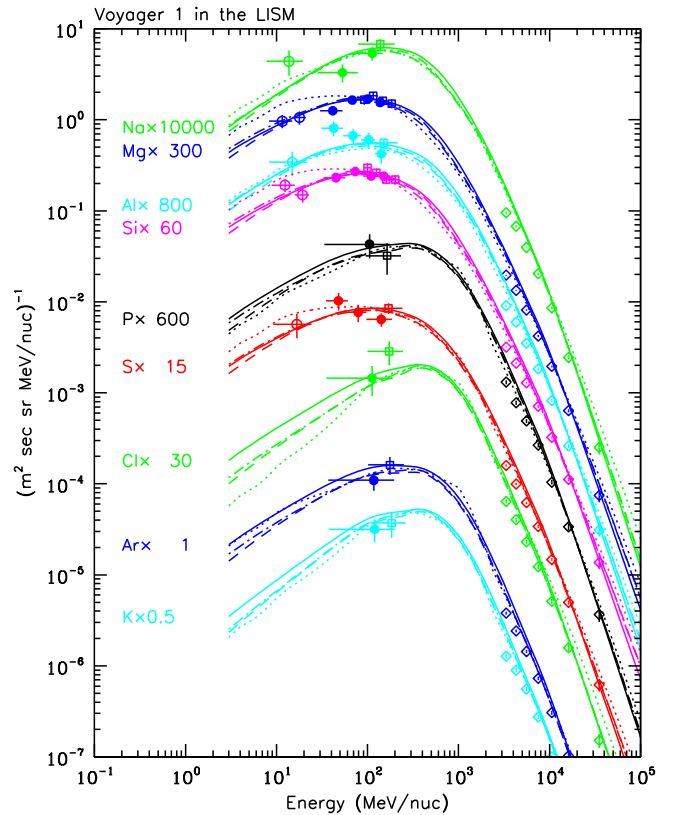


Figure 5. Similar to Figure 4 except for the elements Na through K.

observed energy spectra and the model spectra of Na through K and of Ca through Ni are shown in Figures 5 and 6, respectively.

The *V1* GCR observed abundances relative to Si at 80 MeV nuc $^{-1}$ are shown in Table 3 for all elements from H through Ni, except for Co, for which we have no detection. Ratios of the model intensities at 80 MeV nuc $^{-1}$ from the GALPROP DR and PD2 models and from the LBM model to that of the *V1* observed intensities are shown in Figure 7. Most elements show reasonable agreement between observed and model intensities; however, for some of the rarer elements model intensities can differ by factors of up to ~ 2 at lower energies.

4. ENERGY SPECTRA, ELECTRONS

The *V1* CRS telescopes do not have the capability of distinguishing between e^+ (positrons) and e^- particles. For *V1*, we thus use the term “electron” to mean $e^- + e^+$. The left panel of Figure 8 shows the energy spectrum of GCR electrons derived from *V1* observations, together with a subset of AMS-02 (Aguilar et al. 2014b) electron intensities, also $e^- + e^+$, at high energies that are not that strongly affected by solar modulation. Based on the analysis described in the Appendix, the power law that best fits the *V1* data is $J = (246 \pm 9) (E/10)^{-1.30 \pm 0.05}$, where E is energy in MeV and J is the intensity in units of $(\text{m}^2 \text{ sr MeV})^{-1}$.

Also shown are several model LISM electron spectra. For the case of the Strong et al. (2011) electron energy spectrum, we have added the e^- and e^+ intensities shown in their Figure 1 for a -1.6 injection spectrum to form the equivalent $e^- + e^+$ spectrum that the *V1* and AMS-02 data represent. For the other

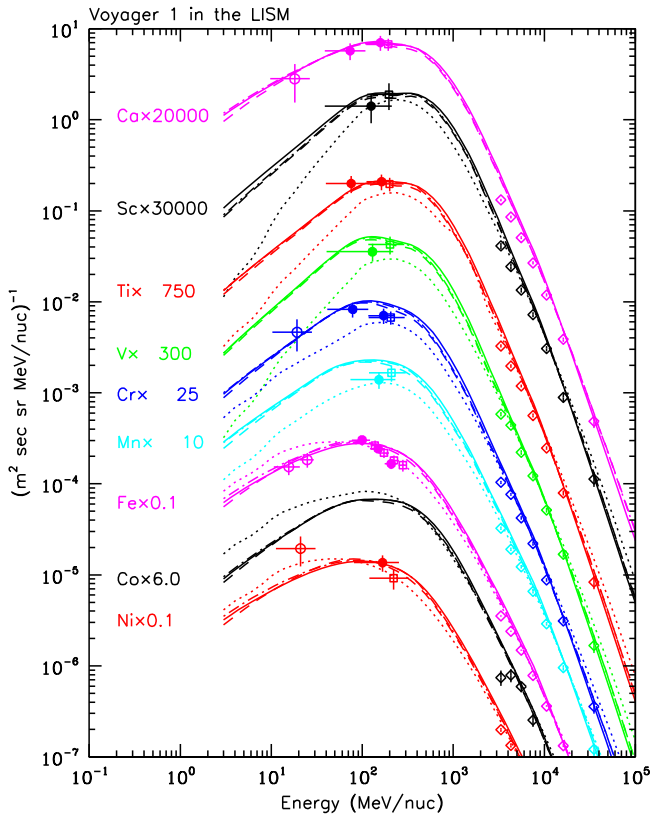


Figure 6. Similar to Figure 4 except for the elements Ca through Ni.

model LISM spectra in Figure 8, what the term electron means was not made explicitly clear in the papers. We note that at the high energies of the AMS-02 data shown in Figure 8, the positron fraction is small, $\leq 6\%$ (Aguilar et al. 2014a). However, the model e^- and e^+ LISM energy spectra of Strong et al. (2011) show that the positron fraction increases toward low energies and is 36% at 100 MeV, for example.

For the purposes of calculating the GCR energy density and the ionization rate of atomic H due to GCRs in this paper, we need to select a model electron energy spectrum that represents the sum of e^- and e^+ intensities in the LISM and extends down to 3 MeV. Although the LISM electron energy spectrum of Potgieter et al. (2015) may have been intended to be an e^- energy spectrum, because the paper treats the modulation of electrons in that paper as if they were negatively charged, the energy spectrum does have the property that it agrees reasonably well with the VI data at low energies and the AMS-02 data at high energies, both of which are $e^- + e^+$ data. We note that the average power-law index of the Potgieter et al. (2015) energy spectrum over the energy range of the VI measurements is -1.36 , in reasonable agreement with the -1.30 ± 0.05 value we find for the VI data. Therefore, we will treat the Potgieter et al. (2015) electron energy spectrum as if it were an $e^- + e^+$ LISM energy spectrum and use it in our calculations of energy density and ionization rate.

In the right panel of Figure 8 we compare the electron and proton energy spectra. We note that at 10 GeV the electron intensity is a small fraction of the proton intensity and the e/p ratio is ~ 0.01 . However, below ~ 50 MeV, the electron intensity exceeds that of protons and by 3 MeV, the e/p intensity ratio is ~ 50 .

Table 3
Voyager 1 GCR Abundances Relative to Si at 80 MeV nuc⁻¹

Element	Nuclear Z	Abundance	Uncertainty	Method
H	1	5.27e+06	4.55e+05	2
He	2	4.29e+05	3.40e+04	2
Li	3	514	105	2
Be	4	231	34	2
B	5	1137	141	2
C	6	8807	763	2
N	7	1288	127	2
O	8	8273	748	2
F	9	27	7	2
Ne	10	794	108	2
Na	11	94	14	2
Mg	12	1193	117	2
Al	13	174	26	2
Si	14	1000	70	2
P	15	16	5	1
S	16	110	24	2
Cl	17	10	4	1
Ar	18	24	6	1
K	19	14	4	1
Ca	20	63	12	2
Sc	21	10	4	1
Ti	22	58	12	2
V	23	27	6	1
Cr	24	71	14	2
Mn	25	30	6	1
Fe	26	607	65	2
Ni	28	34	6	2

Note. The column entitled “Method” refers to how many points were involved in an interpolation to 80 MeV nuc⁻¹. Method 1 is based on only one observation; method 2 uses a power-law interpolation from two points that bracket 80 MeV nuc⁻¹. The observed Si intensity at 80 MeV nuc⁻¹ is $(4.61 \pm 0.32) \times 10^{-3}$ (m² s sr MeV nuc⁻¹)⁻¹. Uncertainties shown are statistical uncertainties and 5% point-to-point systematic uncertainties added in quadrature.

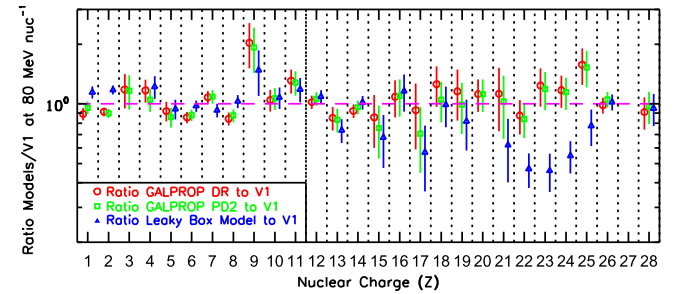


Figure 7. Ratios of model intensities to VI observed intensities at 80 MeV nuc⁻¹. The data are plotted with the statistical and systematic uncertainties added in quadrature.

5. ACCOUNTING FOR THE PENH RATE

The model interstellar electron spectrum of Potgieter et al. (2015) and the model spectra in Figures 3–6 have been selected to be used to calculate the energy density of cosmic rays and the cosmic-ray ionization rate of atomic H by cosmic rays in the LISM. In this section we address the question of whether or not these energy spectra, when integrated and combined with the appropriate geometry factors of the HET 2 telescope, are able to reproduce for the period 2012/342–2105/181 a direct measurement of the integral intensity of GCRs, which is the PENH rate shown in Figure 1. That rate is 2.82 s⁻¹. The results

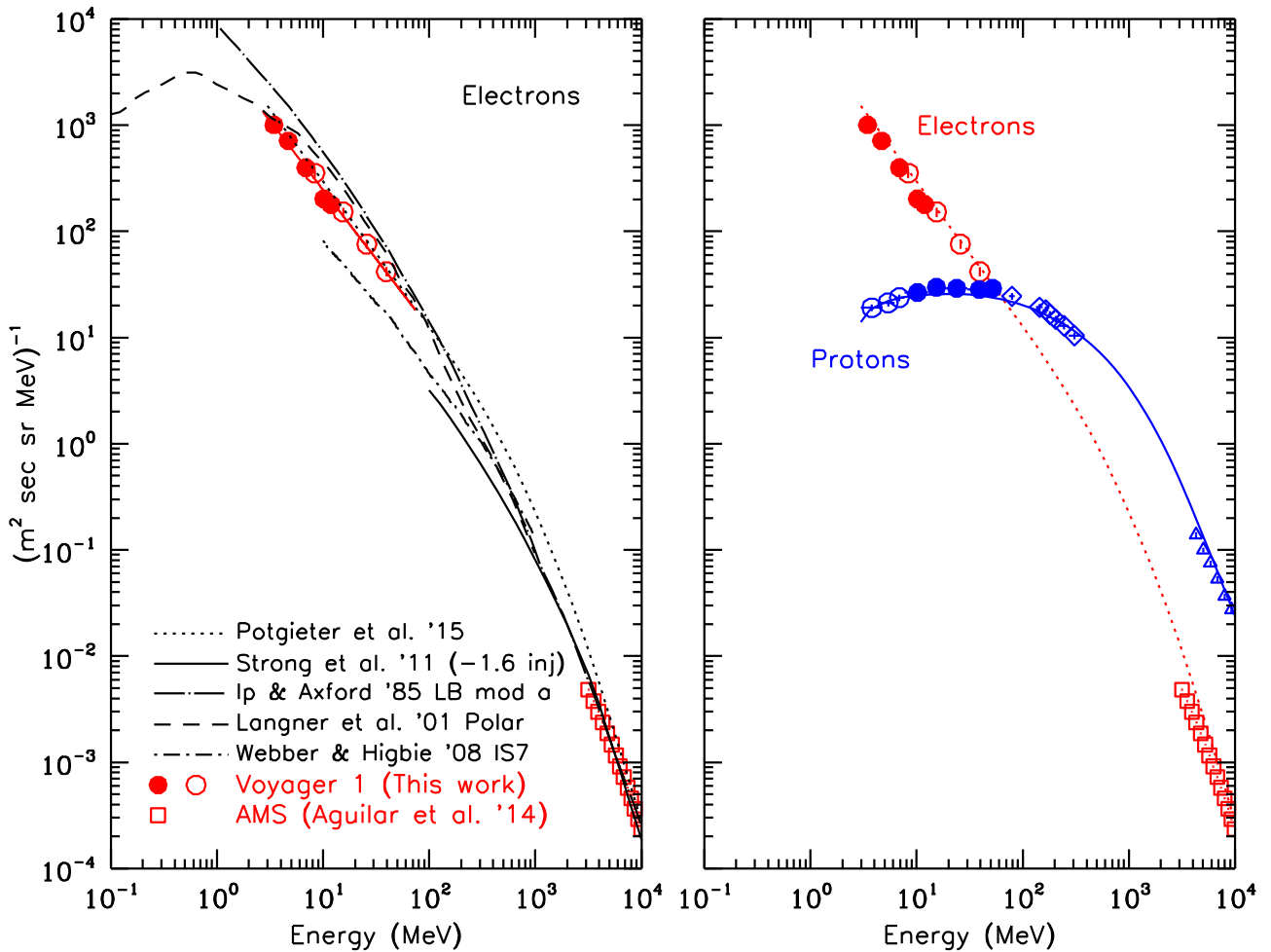


Figure 8. Left panel: energy spectrum of electrons as derived from TET and HET BSe data from the CRS instrument on *VI* ($e^- + e^+$) for the period 2012/342–2015/181 (see the Appendix for more information). Results from the TET telescope are shown as open circles and are derived using response functions based on simulations using the GEANT4 code (Agostinelli et al. 2003; Allison et al. 2006; also see www.geant4.cern.ch). Results from the HET telescope are shown with closed circles, which were also derived using response functions from GEANT4 simulations. A power-law function was fit to the data and the resulting fit is shown as the solid line. The data points are placed at the appropriate energies based on the response functions used in the procedure. Five different estimates of the interstellar energy spectra of electrons are also shown: Strong et al. (2011), Potgieter et al. (2015), Ip & Axford (1985), Langner et al. (2001), and Webber & Higbie (2008). The data at higher energies ($e^- + e^+$, open squares) are from the AMS-02 mission at 1 AU from 2011 May 19 through 2013 November 26 (Aguilar et al. 2014b). The *Voyager* data are tabulated in Table 10. Right panel: the *VI* electron and proton data are repeated from the left panel (electrons) and from Figure 3 (protons). At higher energies data are also repeated and the proton data from BESS is further restricted to show only the region that is not significantly modulated. The dotted curve is the estimated LISM electron spectrum from Potgieter et al. (2015). The solid curve is the calculated LISM proton spectrum from the GALPROP DR model.

are shown in Table 4. The PENH rate is reproduced within 7% for all models, with the GALPROP DR model in combination with the electrons coming closest to accounting for the rate. However, the uncertainty in this type of calculation is large enough, perhaps 10%, that all models are considered equally good in respect to accounting for the PENH rate.

The largest contributors to the PENH rate are protons and electrons. Protons account for $\sim 70\%$ of the rate and electrons account for $\sim 25\%$. The median energy of the rate ranges from 380 to 540 MeV nuc $^{-1}$ for the proton contribution and is 60 MeV for the electron contribution.

The PGH rate⁶ is closely related to the PENH rate and the same electron fraction and median energies of the PENH rate would apply to the PGH rate. The PGH rate is the same as the PENH rate except some PENH particles are rejected when the guard ring around the central active area of the *C1* detector is triggered. We note that the electron fraction and median energies only apply for the period when *VI* is in the LISM.

Table 4
Composition of Observed PENH Rate = 2.82 s^{-1}

Propagation Model for Nuclei	Calculated PENH Rate (s^{-1})					
	H	He	Li-Ni	<i>e</i>	Total	Ratio
LBM	1.83	0.11	0.009	0.75	2.69	0.95
DR	1.98	0.13	0.011	0.75	2.86	1.01
PD1	2.14	0.12	0.010	0.75	3.02	1.07
PD2	2.14	0.12	0.010	0.75	3.01	1.07

Note. The electron rate is the same for each nuclei model listed and is calculated from the LISM electron spectrum of Potgieter et al. (2015) using the response function for electrons penetrating the HET telescope shown in Figure 17. The geometry factors used in calculating the nuclei rates are $1.68 \text{ cm}^2 \text{ sr}$ for H and $1.50 \text{ cm}^2 \text{ sr}$ for $Z > 1$ nuclei. The beginning energy of the integration for all nuclei was 70 MeV nuc $^{-1}$. The column labeled “Ratio” is the ratio of the calculated rate to the observed rate of 2.82 s^{-1} .

The good agreement between the calculated and observed PENH rate gives us confidence that the model LISM energy spectra used in this paper are reasonably accurate.

⁶ Available at <http://voyager.gsfc.nasa.gov/heliopause/recenthist.html>.

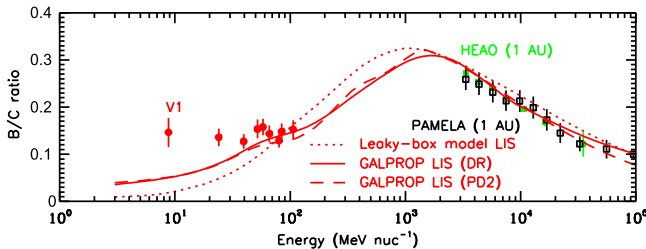


Figure 9. Ratio of B to C from *V1* (this work), *HEAO-3* (Engelmann et al. 1990), and *PAMELA* (Adriani et al. 2014), together with results from three of the models. For the *Voyager* data, the uncertainties reflect statistical uncertainty and the 5% point-to-point systematic uncertainty added in quadrature.

6. B/C RATIO

The B/C ratio is an important ratio in the study of the propagation of GCRs and it has been a difficult ratio to fit with models at energies below a few hundred MeV nuc⁻¹ (Lave et al. 2013). In Figure 9 we show the B/C ratio over a broad energy range, with the new *Voyager* data extending the energy of measurement down to ~ 8 MeV nuc⁻¹. Also shown are a subset of measurements at 1 AU from *HEAO-3* (Engelmann et al. 1990) and *PAMELA* (Adriani et al. 2014) at energies above 3 GeV nuc⁻¹ where modulation effects should be relatively small. Three model results are also shown in the figure, two from the GALPROP models and one from the LBM model, and all three generally show somewhat lower ratios than the *Voyager* observations below ~ 50 MeV nuc⁻¹.

In particular, the data for the lowest-energy point in Figure 9 is from the LET C and D telescopes and the point lies $\sim 3\sigma$ above the GALPROP DR and PD2 models and $\sim 4\sigma$ above the LBM model. We do not believe that this is due to a background problem in the observations. In Figure 10 we show the B, C, N, and O data plotted as the difference of two semi-independent determinations of the nuclear charge, Z1 and Z2, versus the average charge determination, before and after selection of the data. We note that the charge resolution is excellent with essentially no background present.

Some additional model tuning will be required to fully explain the B/C ratios observed in the LISM. Similar difficulties were discussed for the *ACE* data by Lave et al. (2013).

7. GCR ELEMENTAL SOURCE ABUNDANCES

The four models presented in this paper have isotopic source injection spectra as input. For the LBM model, all injection spectra are single power-laws in rigidity and the source abundances are defined in terms of the ratio of spectral intensities to that of ²⁸Si. As described in the Appendix, for a given GALPROP model the injection spectra for all $Z > 2$ nuclei have the same rigidity-dependent source spectra, a double or triple power law in rigidity. The GCR isotopic source abundances for these isotopes are defined by a ratio of spectral intensities at a rigidity of 10 GV. In the case of H and He for the GALPROP models, the triple power laws in rigidity have different spectral indices and different rigidity break points from each other and from the $Z > 2$ nuclei. Thus the concept of GCR isotopic source abundances for H and He from the GALPROP models is not straightforward.

We have summed the GCR isotopic source ratios as described above for each element from the models to form GCR elemental source ratios and these are shown in Table 5. For the case of the

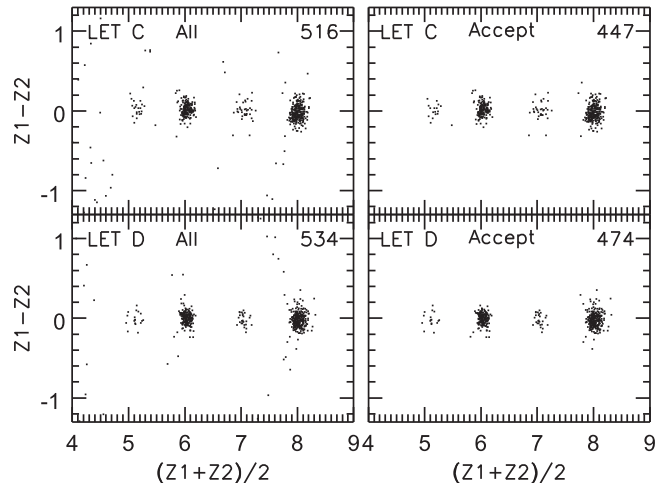


Figure 10. Plot of two semi-independent determinations of the charge of each nucleus vs. the average of the two determinations for B, C, N, and O nuclei, demonstrating the clean separation of these elements in the LET telescopes. The two left panels show all of the data and the two right panels show the data after cuts are applied to remove background. The background is insignificant. See the Appendix for more details of the data analysis technique.

LBM model and for $Z > 2$ for the GALPROP models, these ratios are considered the GCR elemental source abundances. For the GALPROP models, the ratios shown in Table 5 together with the information in Table 12 in the Appendix allows one to reconstruct the injection spectra for H and He, as well as for the other elements.

The fitting technique used in deriving the source abundances for the three GALPROP models result in uncertainties, which are shown for each element in Table 5. These uncertainties do not take into account uncertainties common to the GALPROP models, such as the cross-sections for nuclear interactions. From model to model, the formal fitting uncertainties vary significantly and are in some cases very small compared to the differences in the abundances between the models. We believe that by averaging the abundances derived from four models, three from GALPROP and one from the LBM, we take into account possible uncertainties associated with interstellar propagation and underlying data sets, such as the isotopic production cross-sections. These unweighted means and variances, which we recommend be used as the uncertainties of the elemental source abundances, are shown in the two right-most columns of Table 5.

In Figure 11 we compare the mean elemental source abundances derived in this way to GCR elemental source abundances from *HEAO-3* (Engelmann et al. 1990) and *Ulysses* (Duvernois & Thayer 1996) for the elements reported from those missions where the abundances were finite and not upper limits. We note that the *HEAO* and *Ulysses* abundances assumed injection spectra as single power laws in momentum per nucleon, which is a different form from the GALPROP and LBM models presented here. Nonetheless, in general, the previous and new GCR source abundances are in reasonable agreement where they are determined, with the new source abundances reported here generally showing smaller uncertainties.

8. IONIZATION RATE OF ATOMIC H IN THE LISM BY GALACTIC COSMIC RAYS

The ionization rate of atomic H in the LISM by cosmic rays in units of s⁻¹ is calculated based on Equation (10) of Indriolo

Table 5
Model Elemental Source Ratios at 10 GV

Z	Relative Ratios, $X_Z (X_{\text{Si}} = 100)$					
	DR	PD1	PD2	LBM	Mean	Variance
1	2.41e+04	2.48e+04	2.53e+04	2.44e+04
2	8.46e+03 \pm 5.23e+01	1.02e+04 \pm 1.51e-01	1.04e+04 \pm 1.51e-01	1.04e+04
3	1.25e+00 \pm 1.24e+00	2.66e+00 \pm 1.88e-01	2.09e+00 \pm 1.82e-01	...	2.00	0.71
4	6.29e-07 \pm 1.21e-01	4.92e-11 \pm 7.05e-02	4.21e-12 \pm 6.91e-02	0.00e+00	0.00	0.00
5	2.27e-07 \pm 4.01e-01	3.27e-11 \pm 9.63e-02	4.04e-11 \pm 9.52e-02	0.00e+00	0.00	0.00
6	4.02e+02 \pm 3.23e+00	4.20e+02 \pm 1.66e-01	4.20e+02 \pm 1.64e-01	3.96e+02	409	13
7	3.37e+01 \pm 1.70e+00	3.79e+01 \pm 2.49e-01	3.74e+01 \pm 2.45e-01	3.76e+01	36.7	2.0
8	4.99e+02 \pm 3.87e+00	5.12e+02 \pm 1.99e-01	5.12e+02 \pm 1.96e-01	5.21e+02	511	9
9	4.09e-08 \pm 1.11e-02	6.92e-12 \pm 8.47e-03	4.84e-15 \pm 8.48e-03	2.53e-02	0.01	0.01
10	5.76e+01 \pm 1.20e+00	5.81e+01 \pm 3.01e-01	5.81e+01 \pm 2.97e-01	5.85e+01	58.1	0.4
11	3.88e+00 \pm 1.98e-01	3.91e+00 \pm 1.30e-01	3.88e+00 \pm 1.29e-01	4.41e+00	4.02	0.26
12	1.11e+02 \pm 1.83e+00	1.12e+02 \pm 3.06e-01	1.12e+02 \pm 3.01e-01	1.10e+02	111.0	1.1
13	1.02e+01 \pm 2.24e-01	9.99e+00 \pm 1.42e-01	1.00e+01 \pm 1.40e-01	8.42e+00	9.66	0.83
14	1.00e+02 \pm 9.76e-01	1.00e+02 \pm 2.74e-01	1.00e+02 \pm 2.71e-01	1.00e+02	100	0
15	9.06e-01 \pm 6.23e-02	7.44e-01 \pm 5.79e-02	7.47e-01 \pm 5.77e-02	4.27e-01	0.71	0.20
16	1.33e+01 \pm 5.40e-01	1.29e+01 \pm 2.37e-01	1.29e+01 \pm 2.35e-01	1.31e+01	13.1	0.2
17	5.23e-01 \pm 1.55e-01	2.75e-01 \pm 9.33e-02	2.79e-01 \pm 9.82e-02	1.38e-01	0.30	0.16
18	2.08e+00 \pm 2.92e-01	1.88e+00 \pm 1.79e-01	1.88e+00 \pm 1.79e-01	1.66e+00	1.87	0.17
19	4.61e-01 \pm 1.79e-01	2.26e-01 \pm 1.10e-01	2.43e-01 \pm 1.14e-01	3.37e-01	0.32	0.11
20	6.40e+00 \pm 3.85e-01	6.21e+00 \pm 1.69e-01	6.24e+00 \pm 1.69e-01	...	6.28	0.10
21	1.33e-01 \pm 6.63e-02	6.24e-02 \pm 5.72e-02	6.81e-02 \pm 5.74e-02	4.57e-03	0.07	0.05
22	9.67e-01 \pm 4.00e-01	9.63e-01 \pm 2.40e-01	9.51e-01 \pm 2.36e-01	3.04e-01	0.80	0.33
23	1.03e-01 \pm 2.70e-01	1.43e-01 \pm 1.19e-01	1.20e-01 \pm 1.15e-01	3.68e-02	0.10	0.05
24	3.32e+00 \pm 6.25e-01	3.61e+00 \pm 2.81e-01	3.53e+00 \pm 2.90e-01	2.45e+00	3.23	0.53
25	3.38e+00 \pm 2.61e-01	3.32e+00 \pm 1.89e-01	3.29e+00 \pm 1.87e-01	1.11e+00	2.77	1.11
26	1.09e+02 \pm 1.24e+00	1.10e+02 \pm 3.69e-01	1.10e+02 \pm 3.64e-01	1.17e+02	111.3	3.8
27	1.96e-01 \pm 2.24e-02	1.95e-01 \pm 2.20e-02	1.94e-01 \pm 2.18e-02	4.09e-01	0.25	0.11
28	5.99e+00 \pm 1.93e-01	5.98e+00 \pm 1.54e-01	5.95e+00 \pm 1.53e-01	6.15e+00	6.02	0.09

Note. Source ratios are defined at a common rigidity of 10 GV. For all but H and He of the GALPROP models, these ratios are considered the source abundances. The GALPROP H and He injection spectra do not have the same shape as the GALPROP $Z > 2$ injection spectra. The parameters of the GALPROP H and He injection spectra are listed in Table 12. The column labeled “Mean” is the unweighted average of the models. The column labeled “Variance” is defined as $\sqrt{\sum(x_i^2 - \mu^2)/(N - 1)}$, where x_i is one of the model values, μ is the mean, and N is the number of models involved in the average.

et al. (2009):

$$\zeta_H = 4\pi\xi_H \int_{E_{\text{low}}}^{E_{\text{high}}} J(E)\sigma(E)dE \quad (1)$$

where $\xi_H = 1.5$ to account for ionization due to secondary electrons produced in the initial ionizing event (Glassgold & Langer 1974) and E_{low} is 3 MeV for GCR protons and electrons and 3 MeV nuc $^{-1}$ for GCR nuclei with $Z > 1$. The values of E_{high} were 1.0×10^6 MeV for electrons, 1.07×10^9 MeV nuc $^{-1}$ for the GALPROP nuclei models, and 1.0×10^7 MeV nuc $^{-1}$ for the LBM. $J(E)$ is the differential energy spectrum of the GCR ionizing species and $\sigma(E)$ is the energy-dependent cross-section.

The cross-section, σ , used is the Bethe-Bloch formulation (Bethe 1933, p. 273), which is valid at the relatively high energies used here. The equation for σ in cm 2 as presented in Spitzer & Tomasko (1968) is

$$\sigma = 1.23 \times 10^{-20} Z^2 [6.2 + \log_{10}(\beta^2/(1 - \beta^2)) - 0.43\beta^2]/\beta^2 \quad (2)$$

where Z is the charge of the ionizing particle and βc is the particle velocity.

At energies significantly lower than the V1 measurements, the Bethe-Bloch formula overestimates the cross-section. In

Figure 12 we show the cross-section for ionizing atomic H by GCR protons and He nuclei with energies 10^{-5} MeV nuc $^{-1}$ to 10^6 MeV nuc $^{-1}$, where for values of $\beta < 0.026$ we show the cross-section formulation adapted for ionization of H from Kaganovich et al. (2004) given in cm 2 for an incident ion of charge Z and velocity v in cm s $^{-1}$:

$$\sigma = 4\pi a_0^2 Z^2 G[v/(2.19 \times 10^8 \sqrt{Z + 1})] \quad (3)$$

where $a_0 = 5.29 \times 10^{-9}$ and the function G is given by

$$G(x) = \exp(-1/x^2)[1.26 + 0.283 \ln(2x^2 + 25)]/x^2. \quad (4)$$

Also shown in Figure 12 is the cross-section for ionizing atomic H by GCR electrons, where for electron energies $E < 1000$ eV we use the cross-section formulation of Lotz (1967a, 1967b) as presented in Bzowski et al. (2013):

$$\sigma = 4 \times 10^{-14} [1 - 0.6 e^{-0.56(E/13.6 - 1)}] \frac{\ln(E/13.6)}{13.6E}. \quad (5)$$

The resulting ionization rates, including contributions from GCR electrons, are shown in Table 6. In Figure 13 we show the dependence on nuclear charge of the ionization rate of atomic H. GCR H and He dominate the total rate and only seven elements contribute more than 1% to the total. The total cosmic-ray ionization rate varies from 1.51×10^{-17} to 1.64×10^{-17} s $^{-1}$, which is a factor of 11–12 lower than the

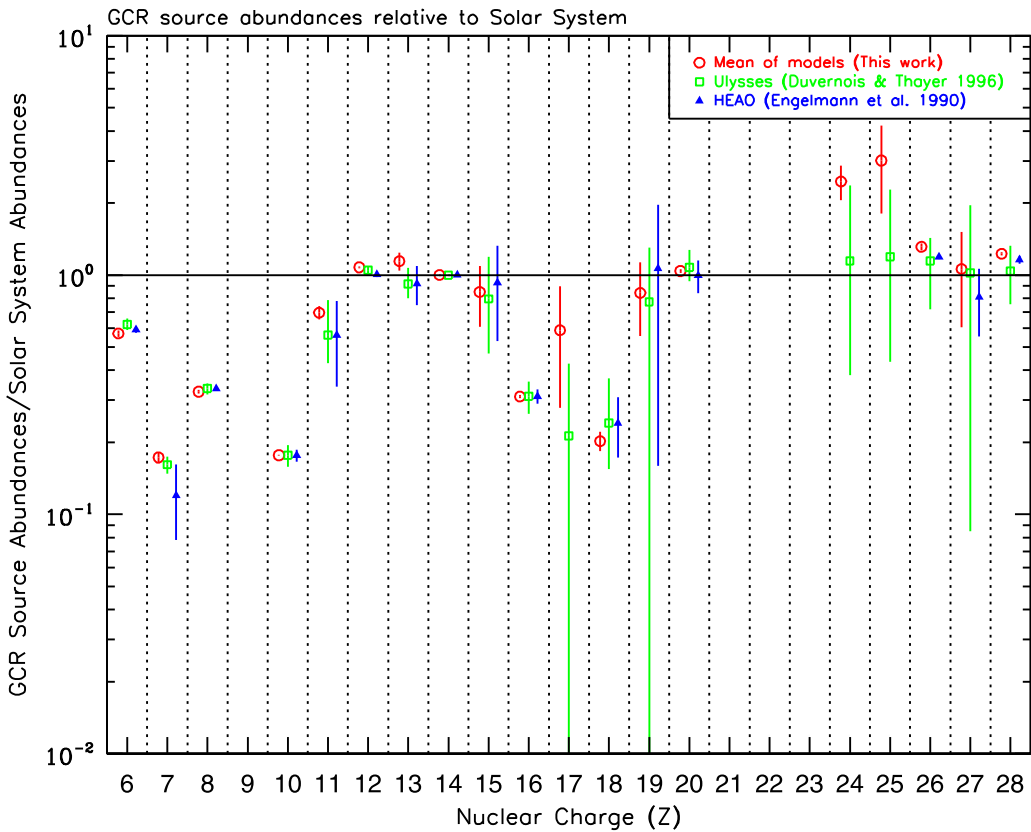


Figure 11. GCR elemental source abundances relative to solar system abundances as described in the text. The solar system abundances are taken from Table 6 of Lodders et al. (2009) and their uncertainties have not been taken into account in forming the ratios.

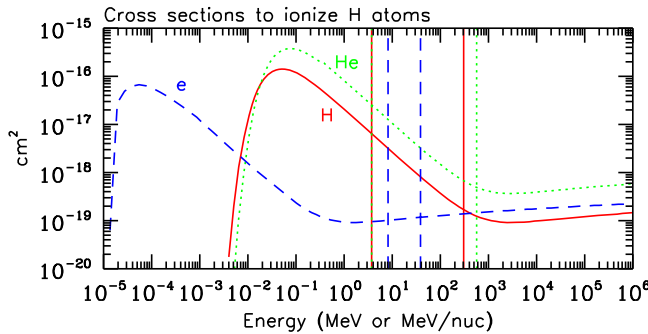


Figure 12. Cross-section in cm^2 for ionization of atomic H by energetic electrons, H ions, and He ions. The curves are from Equations (2)–(5). The vertical lines represent the energy range of the V1 observations with solid being for H, dotted for He, and dashed for electrons.

average cosmic-ray ionization rate of $1.78 \times 10^{-16} \text{ s}^{-1}$ inferred using astrochemistry methods for diffuse interstellar clouds (Indriolo et al. 2015).

9. ENERGY DENSITY

The equation for calculating energy density in eV cm^{-3} is adapted from Indriolo et al. (2009) and is given by

$$\epsilon_{\text{GCR}} = 4\pi N \int_{E_{\text{low}}}^{E_{\text{high}}} E (J(E)/v) dE \quad (6)$$

where v is the particle velocity in cm s^{-1} and the intensity $J(E)$ is in $(\text{cm}^2 \text{s sr eV})^{-1}$ for protons and electrons, where $N = 1$, and in $(\text{cm}^2 \text{s sr eV nuc}^{-1})^{-1}$ for heavier ions with N being the

number of nucleons. The limits of integration are as in Equation (1), except eV and eV nuc^{-1} are the units used instead of MeV and MeV nuc^{-1} .

The resulting energy densities, including contributions from GCR electrons, are shown in Table 6. We find that the total energy density among the models ranges from 0.83 to 1.02 eV cm^{-3} .

Similar to Figure 13 we show in Figure 14 the energy densities of the different GCR nuclei. GCR H and He are dominant with just four nuclei contributing more than 1% of the total.

We note that the dominant contribution to the energy density occurs above the energy range of the *Voyager* observations as shown in Figure 15. While the *Voyager* observations are important to constrain the possible interstellar spectra at the low energies, we rely on model spectra to bridge the gap between the *Voyager* observations and the high-energy, 1 AU, approximately unmodulated observations.

10. DISCUSSION

The new *Voyager* observations in the LISM reported here show that the gradient of protons is very low, consistent with zero with a 1σ upper limit of $0.06\% \text{ AU}^{-1}$. Whether or not there should be a gradient in the LISM has been a subject of debate, with several researchers claiming there should be a positive radial gradient beyond the heliopause (Scherer et al. 2011; Herbst et al. 2012; Strauss et al. 2013; Strauss & Potgieter 2014) and others claiming there should be no gradient at all (Jokipii 2001; Guo & Florinski 2014; Kóta & Jokipii 2014). For example, Strauss & Potgieter (2014) argue that protons with 100 MeV should increase by 25% to 40% over a

Table 6
Energy Density and Ionization Rate of Atomic H

Propagation Model for Nuclei	Energy Density, eV cm ⁻³					Ionization Rate, 10 ⁻¹⁷ s ⁻¹				
	H	He	Li–Ni	e	Total	H	He	Li–Ni	e	Total
LBM	0.58	0.15	0.07	0.04	0.83	0.85	0.27	0.28	0.23	1.64
DR	0.71	0.18	0.07	0.04	1.00	0.76	0.24	0.28	0.23	1.51
PD1	0.73	0.17	0.07	0.04	1.02	0.83	0.24	0.28	0.23	1.56
PD2	0.73	0.17	0.07	0.04	1.01	0.83	0.24	0.27	0.23	1.56

Note. In calculating these quantities, the energy interval for integration was 3 MeV to 10⁶ MeV for electrons, 3 MeV nuc⁻¹ to 1.07 × 10⁹ MeV nuc⁻¹ for the GALPROP models, and 3 MeV nuc⁻¹ to 10⁷ MeV nuc⁻¹ for the LBM model.

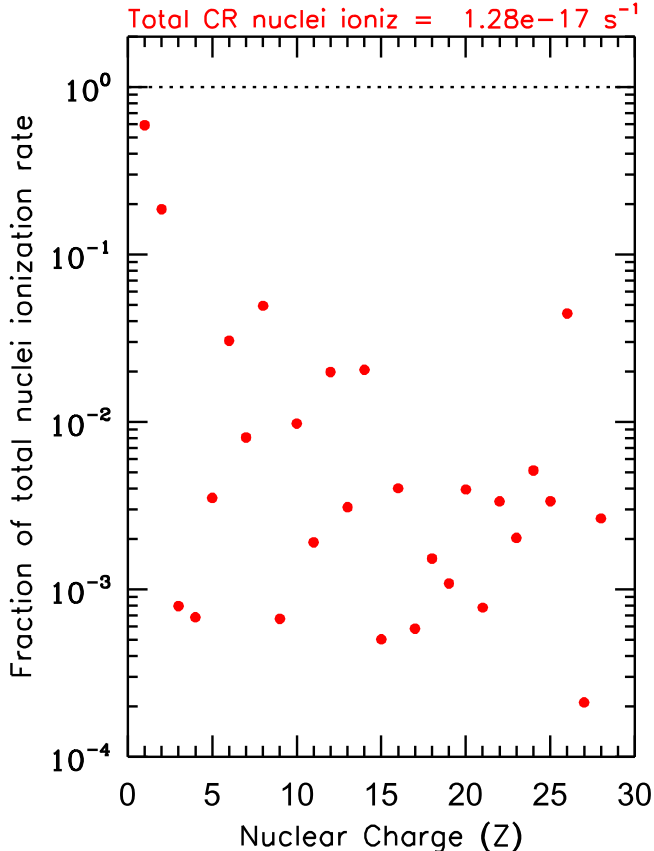


Figure 13. Ionization rate from GCR nuclei relative to the total GCR-nuclei-induced ionization rate of atomic H based on the GALPROP DR model of the interstellar energy spectra.

100 AU distance beyond the heliopause, corresponding to an average gradient of 0.25% AU⁻¹ to 0.4% AU⁻¹. Our result of a radial gradient with a 1 σ upper limit of 0.06% AU⁻¹ suggests that the *V1* energy spectra of GCRs observed during the period 2012/342–2015/181 represent the unmodulated energy spectra present in the LISM. We note that Zhang et al. (2015) and Luo et al. (2015) arrived at the same conclusion and presented evidence that the modulation boundary is likely only a fraction of an AU beyond the heliopause.

These new observations have revealed the low-energy part of the LISM energy spectrum for the first time. All previous observed spectra were modified from the spectra in the LISM by solar modulation effects. The solar modulation effects include adiabatic deceleration, so that the GCR particles that are observed inside the heliosphere typically had much higher energies in the LISM by a few hundred MeV nuc⁻¹. In

addition, for many elements, heliospheric particles, particularly those from the anomalous component, completely obscured the GCRs below \sim 100 MeV nuc⁻¹ when the spacecraft was inside the heliosphere.

The LISM energy spectra of nuclei are found to flatten and roll over below a few hundred MeV nuc⁻¹, as compared to the approximate power-law energy dependence at higher energies with negative power-law indices. The H and He spectra have the same spectral shape from 3–346 MeV nuc⁻¹ with the peak intensity falling within 10–50 MeV nuc⁻¹. A common spectral shape in the vicinity of the peak intensity would not be expected from solar modulation effects for two species with a mass-to-charge ratio differing by a factor of two. The *V1* observations are thus consistent with the proposition that the energy spectra are from the LISM.

We have produced a new table of elemental GCR source abundances (Table 5) based on the average of four different models of the propagation of GCRs from their source, which are newly constrained by the *Voyager* observations. This new table should prove helpful in studies trying to identify the source of GCRs.

The LISM electron spectrum appears to have flattened and rolled over below a few hundred MeV; however, the peak intensity is at lower energies than that of the nuclei and apparently below the limit of the energy range of the *Voyager* CRS HET (2.7 MeV). At these low energies the ionization energy losses are much less for electrons than for protons of the same energy, so the observations are not unexpected. Nonetheless, the new observations will help constrain propagation parameters in future modeling efforts.

We note that contrary to the situation at high energies, the electron intensity exceeds that of protons below \sim 50 MeV. At 3 MeV, the proton intensity is only \sim 2% of the electron intensity. While previous models indicated that the electron intensity would likely dominate that of protons below \sim 100 MeV (see, e.g., Ip & Axford 1985; Webber 1998), this is the first in situ observation of such an effect and we find the LISM electron–proton intensity cross-over energy is \sim 50 MeV.

The observed B/C ratio from instruments at 1 AU has been difficult to reconcile with models (see, e.g., Lave et al. 2013), and this continues with the new *Voyager* observations in the LISM. From Figure 4, it appears that the observed B energy spectrum is well above the model B energy spectra, whereas the model C energy spectra agree reasonably well with the observations of GCR C. It is likely that some improvement in the cross-sections that produce B is needed for the models to reproduce the observed B energy spectrum at *V1*.

Despite this discrepancy in the B energy spectrum and in some other energy spectra of secondary nuclei, the models are very useful for investigating the ionization rate of atomic H in

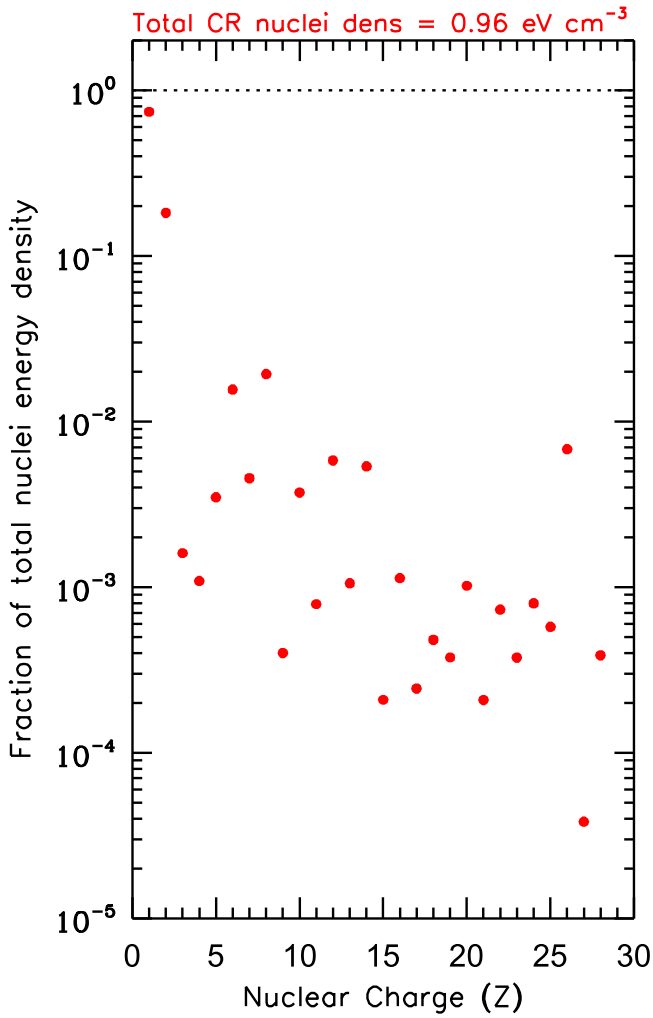


Figure 14. Energy density of GCR nuclei relative to the total GCR nuclei energy density based on the GALPROP DR model of the interstellar energy spectra.

the LISM and in calculating the energy density of GCRs. This is due to the fact that protons and helium are the major contributors to these two quantities and the H and He observations in the LISM are reasonably well matched by the models.

Our result for the ionization rate of atomic H in the LISM by GCR nuclei with energy $>3 \text{ MeV nuc}^{-1}$ and by GCR electrons $>3 \text{ MeV}$ is much lower than deduced by researchers using astrochemistry methods, by a factor of 11–12. As seen in Figure 12 the cross-section for ionization of atomic H peaks at energies much lower than the *V1* observations. Most attempts to resolve the ionization rate discrepancy in the literature involve allowing the then unknown interstellar energy spectra of GCR protons, e.g., to turn up below energies of $\sim 100 \text{ MeV}$ (e.g., Indriolo et al. 2009; Wiedenbeck 2013). However, the new *V1* observations indicate that there is no turn up in the proton spectrum down to at least 3 MeV in the LISM (see, e.g., Figure 3).

On the other hand, the discrepancy is perhaps not particularly surprising for a number of reasons. Among the possibilities to explain the difference is a spatially variable GCR energy spectrum in the Galaxy; especially the larger ionization rate is expected in spiral arms which host GCR

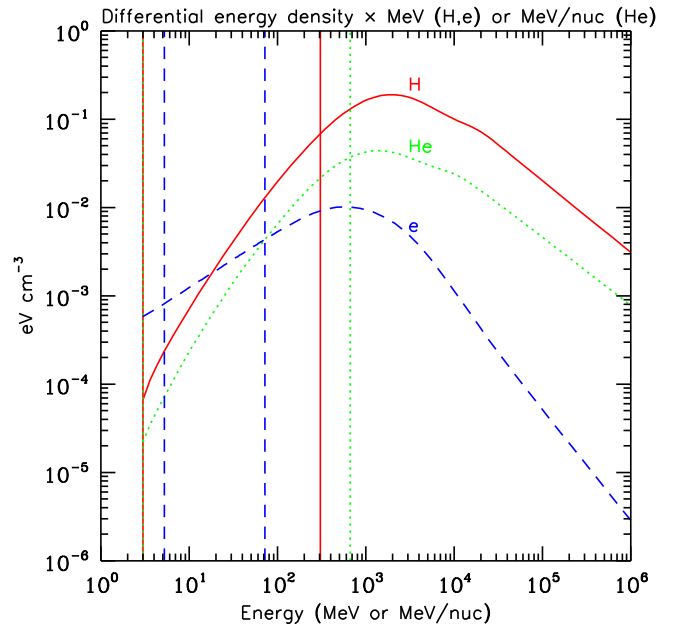


Figure 15. Differential energy density multiplied by energy for H, He, and e vs. energy using the GALPROP DR model for the interstellar energy spectra of H and He and the Potgieter et al. (2015) model of the interstellar electron spectrum. This presentation indicates at what energies the maximum contribution to the energy density arises. Shown as vertical lines are the energy ranges of the *Voyager* observations (solid: H; dotted: He; and dashed: electrons).

sources and thus higher densities of GCRs. Consistent with that hypothesis is that, according to Taillet & Maurin (2003) and Jóhannesson et al. (2016), most of the GCR nuclei that are observed in the LISM originate within a few kiloparsecs from the Sun.

Another possibility: the local interstellar wind may have a suprathermal tail that could contribute to the ionization of atomic H. Suprathermal tails are ubiquitous in the heliosphere and are often attributed to a pump mechanism (Fisk & Gloeckler 2012). We find that, for example, a suprathermal tail on the Maxwell–Boltzmann energy distribution of the interstellar wind of protons with an energy spectrum of $4.4 \times 10^{-3} E^{-1.5} \exp[-E/(0.2 \text{ MeV})] (\text{cm}^2 \text{s sr MeV})^{-1}$ would result in approximately the increase required in the ionization rate of atomic H, with negligible change in the energy density. This is shown in Figure 16. Suprathermal tails of electrons and of the heavier nuclei could contribute to the ionization rate as well. It remains for future work to see if interstellar turbulence is large enough to sustain such suprathermal tails and to explore the other possibilities mentioned above.

The energy density result we report requires an estimate of the LISM spectra across an energy gap in the observations. The four models presented here yield a range of results from 0.83 to 1.02 eV cm^{-3} . To equal this range of energy densities the interstellar magnetic field would have an intensity of $5.8\text{--}6.4 \mu\text{G}$, if there were equipartition. Although the observed intensity in the very LISM is nearly this large, ranging from ~ 4 to $5.5 \mu\text{G}$, this is likely enhanced due to draping around the heliosphere. The unperturbed field is expected to be in the range of $2\text{--}4 \mu\text{G}$ (Burlaga et al. 2015).

We note that the cosmic-ray ionization rate we derive is lower by a factor of ~ 2 than that derived by Webber (1998) ($[3\text{--}4] \times 10^{-17} \text{ s}^{-1}$) and the energy density we derive is also lower than in (Webber 1998) ($\sim 1.8 \text{ eV cm}^{-3}$). We ascribe the

Table 7
Voyager 1 Intensities of H for 2012/342–2015/181

E_{\min} (MeV)	E_{\max} (MeV)	E_{plot} (MeV)	Intensity, J ($\text{m}^2 \text{s sr MeV}^{-1}$)	sig	sys	Counts	Tel Type
3.0	4.6	3.8	1.908e+01	9.572e−01	9.540e−01	59618	1
4.6	6.2	5.4	2.116e+01	1.061e+00	1.058e+00	66114	1
6.2	7.7	6.9	2.369e+01	1.188e+00	1.184e+00	69384	1
7.7	12.8	10.2	2.665e+01	1.345e+00	1.333e+00	21231	2
12.8	17.9	15.4	2.968e+01	1.496e+00	1.484e+00	23585	2
17.9	30.0	23.9	2.909e+01	1.460e+00	1.454e+00	52900	2
30.0	48.0	39.0	2.829e+01	1.419e+00	1.415e+00	67635	2
48.0	56.0	52.0	2.914e+01	1.468e+00	1.457e+00	26293	2
74.5	83.7	79.1	2.443e+01	1.263e+00	1.221e+00	5761	3
132.8	154.9	143.9	1.927e+01	9.723e−01	9.635e−01	21841	3
154.9	174.9	164.9	1.820e+01	9.197e−01	9.100e−01	18635	3
174.9	187.7	181.3	1.652e+01	8.410e−01	8.260e−01	10892	3
187.7	220.5	204.1	1.492e+01	7.519e−01	7.460e−01	25090	3
220.5	270.0	245.3	1.289e+01	6.484e−01	6.445e−01	32802	3
270.0	346.0	308.0	1.042e+01	5.236e−01	5.210e−01	40647	3

Note. The energy range corresponding to the intensity, J , is $E_{\min} - E_{\max}$. Eplot denotes the energy of the plotted points. The “sig” column represents 1σ statistical uncertainties combined in quadrature with a 5% point-to-point systematic uncertainty. This uncertainty was estimated by examining the point-to-point deviations of the data from the smooth LISIM proton spectra from the four models shown in Figure 3. The “sys” column represents an estimated systematic uncertainty of 5% on the absolute intensity that arises due to imprecise knowledge of test capacitors used in the pre-launch calibration procedure. This part of the systematic uncertainty would likely be correlated with other elements and thus should not be applied when taking ratios of intensities. The Tel Type numbers denote from which telescope and mode the data are derived: 1 = LET C, D with slant threshold not triggered. 2 = HET 2 A end stopping particles in high-gain mode. 3 = HET 2 penetrating particles in high-gain mode (see Stone et al. 1977). In Tel Types 1 and 2, two semi-independent determinations of the nuclear charge are formed from energy-loss measurements in three detectors and consistency between the two determinations is required.

Table 8
Voyager 1 Intensities of He for 2012/342–2015/181

E_{\min} (MeV nuc $^{-1}$)	E_{\max} (MeV nuc $^{-1}$)	E_{plot} (MeV nuc $^{-1}$)	Intensity, J ($\text{m}^2 \text{s sr MeV nuc}^{-1}$) $^{-1}$	sig	sys	Counts	Tel Type
3.0	4.6	3.8	1.530e+00	7.964e−02	7.650e−02	4780	1
4.6	6.2	5.4	1.767e+00	9.149e−02	8.835e−02	5521	1
6.2	7.7	6.9	1.936e+00	1.002e−01	9.680e−02	5671	1
7.7	12.8	10.2	2.228e+00	1.233e−01	1.114e−01	1775	2
12.8	17.9	15.4	2.475e+00	1.358e−01	1.238e−01	1967	2
17.9	30.0	23.9	2.563e+00	1.336e−01	1.282e−01	4657	2
30.0	48.0	39.0	2.370e+00	1.226e−01	1.185e−01	5670	2
48.0	56.0	52.0	2.241e+00	1.226e−01	1.120e−01	2022	2
110.2	133.9	122.0	1.746e+00	8.831e−02	8.730e−02	17166	3
133.9	151.7	142.8	1.585e+00	8.059e−02	7.925e−02	11734	3
151.7	193.1	172.4	1.409e+00	7.103e−02	7.045e−02	24182	3
193.1	238.8	216.0	1.184e+00	5.973e−02	5.920e−02	22414	3
238.8	317.8	278.3	9.229e−01	4.645e−02	4.614e−02	30221	3
317.8	381.3	349.5	7.844e−01	3.960e−02	3.922e−02	20669	3
381.3	480.5	430.9	5.954e−01	3.001e−02	2.977e−02	24487	3
480.5	661.4	571.0	4.235e−01	2.131e−02	2.118e−02	31770	3

Note. See notes for Table 7 except Tel Type = 3 are HET 2 penetrating particles from the low-gain mode.

differences to the different interstellar energy spectra used, with the new *VI* GCR electron measurements resulting in a significant reduction of the electron contribution to the ionization rate.

We appreciate discussions with Mark Wiedenbeck and George Gloeckler. *Voyager* data analysis is supported by NASA Grant NNN12AA01C. GALPROP development is supported by NASA Grants NNX13AC47G, NNX10AE78G, NNX16AF27G, and NNX15AU79G.

APPENDIX A DATA ANALYSIS AND MODEL DESCRIPTIONS AND TABLES OF ENERGY SPECTRA AND MODELS

We briefly discuss the analysis techniques used to produce the *Voyager 1* data plotted in the figures, as well as descriptions of the models. We also present tables of the *VI* observations and tables of the model energy spectra we used to compute the energy density of GCRs and ionization rates of atomic H.

The CRS instrument is described in Stone et al. (1977). On each of the *Voyager* spacecraft there are four LETs, referred to

Table 9
Voyager 1 Intensities of $Z > 2$ Nuclei

Z	E_{\min}	E_{\max}	J	sig	sys	Counts	TT	Z	E_{\min}	E_{\max}	J	sig	sys	Counts	TT
3	36.3	44.3	2.08e-03	4.77e-04	1.04e-04	20.0	3	12	8.3	14.9	3.21e-03	5.05e-04	1.61e-04	45.0	1
3	44.3	56.3	2.66e-03	4.75e-04	1.33e-04	34.0	3	12	14.9	20.9	3.53e-03	5.56e-04	1.77e-04	45.0	1
3	56.3	72.5	1.93e-03	3.71e-04	9.63e-05	29.0	3	12	30.0	53.0	4.18e-03	4.20e-04	2.09e-04	132.1	2
3	72.5	88.3	2.38e-03	4.65e-04	1.19e-04	28.0	3	12	53.0	83.0	5.48e-03	4.66e-04	2.74e-04	210.6	2
4	48.0	74.5	8.98e-04	1.82e-04	4.49e-05	26.0	3	12	83.0	118.0	5.63e-03	4.65e-04	2.81e-04	230.8	2
4	74.5	117.2	1.20e-03	1.96e-04	5.99e-05	41.0	3	12	118.0	157.0	5.18e-03	4.48e-04	2.59e-04	201.1	2
5	5.0	12.5	2.14e-03	3.81e-04	1.07e-04	34.0	1	12	82.8	100.5	5.52e-03	5.83e-04	2.76e-04	116.0	3
5	17.0	31.0	4.03e-03	5.00e-04	2.01e-04	77.5	2	12	100.5	129.6	6.11e-03	5.44e-04	3.05e-04	184.0	3
5	31.0	48.0	4.28e-03	4.85e-04	2.14e-04	96.8	2	12	129.6	165.6	5.41e-03	4.90e-04	2.70e-04	175.0	3
5	48.0	68.0	5.95e-03	5.84e-04	2.98e-04	140.2	2	12	165.6	203.3	5.03e-03	5.02e-04	2.51e-04	134.0	3
5	68.0	92.0	5.24e-03	5.38e-04	2.62e-04	124.8	2	13	8.3	21.5	4.28e-04	1.25e-04	2.14e-05	12.0	1
5	46.1	58.0	5.54e-03	6.82e-04	2.77e-04	79.0	3	13	31.0	54.0	1.01e-03	1.86e-04	5.05e-05	31.8	2
5	58.0	74.2	5.57e-03	6.35e-04	2.78e-04	95.0	3	13	54.0	85.0	8.33e-04	1.48e-04	4.17e-05	34.1	2
5	74.2	95.0	5.90e-03	6.28e-04	2.95e-04	113.0	3	13	85.0	121.0	7.51e-04	1.39e-04	3.75e-05	31.4	2
5	95.0	117.3	5.70e-03	6.56e-04	2.85e-04	93.0	3	13	121.0	163.0	5.30e-04	1.18e-04	2.65e-05	21.1	2
6	5.4	6.4	1.79e-02	3.04e-03	8.95e-04	38.0	1	13	87.0	214.0	6.96e-04	8.31e-05	3.48e-05	85.0	3
6	6.4	7.9	1.38e-02	2.19e-03	6.91e-04	44.0	1	14	8.8	15.9	3.19e-03	4.87e-04	1.59e-04	48.0	1
6	7.9	10.3	1.47e-02	1.85e-03	7.36e-04	75.0	1	14	15.9	22.7	2.49e-03	4.34e-04	1.25e-04	36.0	1
6	10.3	14.4	2.02e-02	1.83e-03	1.01e-03	176.0	1	14	33.0	57.0	3.85e-03	3.95e-04	1.93e-04	125.1	2
6	20.0	36.0	3.24e-02	2.03e-03	1.62e-03	711.0	2	14	57.0	90.0	4.48e-03	3.93e-04	2.24e-04	193.7	2
6	36.0	56.0	3.42e-02	2.12e-03	1.71e-03	750.6	2	14	90.0	129.0	4.02e-03	3.61e-04	2.01e-04	180.5	2
6	56.0	80.0	3.88e-02	2.29e-03	1.94e-03	1024.5	2	14	129.0	173.0	3.99e-03	3.67e-04	1.99e-04	167.5	2
6	80.0	106.0	3.83e-02	2.24e-03	1.92e-03	1093.7	2	14	90.2	109.6	4.96e-03	5.27e-04	2.48e-04	114.0	3
6	56.6	68.0	3.89e-02	2.58e-03	1.95e-03	532.0	3	14	109.6	141.0	4.38e-03	4.27e-04	2.19e-04	142.0	3
6	68.0	87.0	4.11e-02	2.51e-03	2.06e-03	825.0	3	14	141.0	180.3	3.66e-03	3.71e-04	1.83e-04	129.0	3
6	87.0	111.5	3.89e-02	2.34e-03	1.95e-03	882.0	3	14	180.3	222.5	3.67e-03	3.96e-04	1.83e-04	109.0	3
6	111.5	137.0	3.39e-02	2.17e-03	1.69e-03	625.0	3	15	33.5	177.0	7.14e-05	2.10e-05	3.57e-06	11.9	2
7	6.6	11.5	2.31e-03	4.85e-04	1.15e-04	24.0	1	15	95.0	233.0	5.35e-05	2.04e-05	2.67e-06	7.0	3
7	11.5	15.5	3.53e-03	6.69e-04	1.77e-04	30.0	1	16	9.2	24.2	3.77e-04	1.10e-04	1.88e-05	12.0	1
7	22.0	39.0	4.75e-03	5.12e-04	2.37e-04	109.4	2	16	35.1	61.0	6.84e-04	1.42e-04	3.42e-05	24.5	2
7	39.0	61.0	5.63e-03	5.28e-04	2.81e-04	158.8	2	16	61.0	97.0	5.11e-04	1.08e-04	2.55e-05	23.6	2
7	61.0	87.0	5.51e-03	5.09e-04	2.76e-04	166.0	2	16	97.0	186.0	4.27e-04	7.10e-05	2.13e-05	39.7	2
7	87.0	114.0	7.32e-03	6.51e-04	3.66e-04	185.2	2	16	99.0	242.0	5.65e-04	7.07e-05	2.83e-05	76.0	3
7	61.0	74.0	5.73e-03	6.71e-04	2.86e-04	89.0	3	17	35.4	189.0	4.83e-05	1.74e-05	2.41e-06	7.8	2
7	74.0	94.8	6.25e-03	6.19e-04	3.13e-04	137.0	3	17	100.0	246.0	9.47e-05	2.67e-05	4.74e-06	13.0	3
7	94.8	121.3	6.19e-03	5.93e-04	3.09e-04	150.0	3	18	37.0	197.0	1.10e-04	2.48e-05	5.48e-06	20.6	2
7	121.3	149.0	6.45e-03	6.55e-04	3.22e-04	128.0	3	18	101.2	251.0	1.61e-04	3.46e-05	8.07e-06	23.0	3
8	7.1	8.5	2.02e-02	2.80e-03	1.01e-03	60.0	1	19	37.6	202.0	6.34e-05	1.79e-05	3.17e-06	12.9	2
8	8.5	10.6	1.66e-02	2.10e-03	8.30e-04	74.0	1	19	106.0	262.0	7.41e-05	2.27e-05	3.71e-06	11.0	3
8	10.6	13.9	2.14e-02	2.05e-03	1.07e-03	150.0	1	20	9.7	26.4	1.41e-04	6.35e-05	7.05e-06	5.0	1
8	13.9	17.0	2.69e-02	2.43e-03	1.34e-03	177.0	1	20	38.8	108.0	2.86e-04	5.80e-05	1.43e-05	25.8	2
8	17.1	21.6	2.86e-02	2.58e-03	1.43e-03	177.8	2	20	108.0	208.0	3.51e-04	6.20e-05	1.76e-05	34.8	2
8	21.6	30.6	3.00e-02	2.17e-03	1.50e-03	365.9	2	20	110.5	275.5	3.38e-04	4.93e-05	1.69e-05	53.0	3
8	30.6	46.0	3.39e-02	2.14e-03	1.69e-03	679.5	2	21	38.9	211.0	4.71e-05	1.65e-05	2.35e-06	8.3	2
8	46.0	66.0	3.37e-02	2.03e-03	1.68e-03	876.8	2	21	113.0	281.0	6.31e-05	2.02e-05	3.16e-06	10.0	3
8	66.0	94.0	3.82e-02	2.19e-03	1.91e-03	1255.8	2	22	39.8	111.0	2.66e-04	5.50e-05	1.33e-05	24.8	2
8	94.0	125.0	3.53e-02	2.07e-03	1.76e-03	1056.5	2	22	111.0	215.0	2.79e-04	5.24e-05	1.39e-05	30.5	2
8	65.7	79.8	3.60e-02	2.32e-03	1.80e-03	606.0	3	22	114.0	284.5	2.62e-04	4.26e-05	1.31e-05	42.0	3
8	79.8	102.5	3.88e-02	2.32e-03	1.94e-03	926.0	3	23	40.4	218.0	1.18e-04	2.52e-05	5.92e-06	23.3	2
8	102.5	131.3	3.48e-02	2.09e-03	1.74e-03	912.0	3	23	116.0	289.0	1.42e-04	3.04e-05	7.08e-06	23.0	3
8	131.3	160.3	3.47e-02	2.16e-03	1.73e-03	718.0	3	24	10.3	28.1	1.85e-04	7.06e-05	9.26e-06	7.0	1
9	25.0	130.0	1.16e-04	3.16e-05	5.80e-06	13.9	2	24	41.1	116.0	3.30e-04	6.01e-05	1.65e-05	32.6	2
9	70.5	172.5	2.93e-04	5.64e-05	1.46e-05	29.0	3	24	116.0	227.0	2.82e-04	5.14e-05	1.41e-05	32.6	2
10	7.7	13.7	1.65e-03	3.69e-04	8.25e-05	21.0	1	24	117.5	293.0	2.68e-04	4.26e-05	1.34e-05	44.0	3
10	13.7	18.7	2.36e-03	4.86e-04	1.18e-04	25.0	1	25	74.0	231.0	1.39e-04	2.84e-05	6.97e-06	25.7	2
10	27.0	48.0	3.08e-03	3.62e-04	1.54e-04	88.4	2	25	119.0	300.0	1.65e-04	3.24e-05	8.27e-06	28.0	3
10	48.0	75.0	3.35e-03	3.51e-04	1.68e-04	118.0	2	26	10.7	20.5	1.54e-03	2.83e-04	7.69e-05	32.0	1
10	75.0	107.0	4.48e-03	4.14e-04	2.24e-04	166.2	2	26	20.5	29.2	1.84e-03	3.29e-04	9.21e-05	34.0	1
10	107.0	140.0	3.66e-03	3.87e-04	1.83e-04	115.3	2	26	77.0	122.0	3.03e-03	2.75e-04	1.51e-04	173.1	2
10	74.6	90.5	3.70e-03	4.79e-04	1.85e-04	70.0	3	26	122.0	177.0	2.43e-03	2.31e-04	1.21e-04	151.7	2
10	90.5	116.2	3.63e-03	4.11e-04	1.82e-04	97.0	3	26	177.0	239.0	1.66e-03	1.87e-04	8.29e-05	97.5	2
10	116.2	149.0	3.51e-03	3.86e-04	1.75e-04	104.0	3	26	123.7	151.3	2.64e-03	3.16e-04	1.32e-04	85.0	3
10	149.0	183.0	3.43e-03	4.14e-04	1.71e-04	83.0	3	26	151.3	195.5	2.19e-03	2.47e-04	1.09e-04	98.0	3
11	7.8	19.6	4.39e-04	1.34e-04	2.20e-05	11.0	1	26	195.5	251.0	1.81e-03	2.14e-04	9.06e-05	87.0	3

Table 9
(Continued)

Z	E_{\min}	E_{\max}	J	sig	sys	Counts	TT	Z	E_{\min}	E_{\max}	J	sig	sys	Counts	TT
11	28.2	78.0	3.30e–04	7.28e–05	1.65e–05	21.7	2	26	251.0	308.5	1.60e–03	2.18e–04	8.00e–05	62.0	3
11	78.0	147.0	5.39e–04	9.00e–05	2.69e–05	39.4	2	28	11.3	30.7	1.94e–04	6.94e–05	9.71e–06	8.0	1
11	79.0	198.0	6.78e–04	8.39e–05	3.39e–05	78.0	3	28	81.0	253.0	1.36e–04	2.74e–05	6.81e–06	26.3	2
...	28	120.0	322.0	9.21e–05	2.28e–05	4.60e–06	17.0	3

Note. Time period for Tel Types (column labeled TT) 1 and 2 is 2012/342–2015/181. Time period for Tel Type 3 is 2012/342–2014/365. Also see notes for Table 7 except for the definitions of Tel Type, which are 1 = LET C, D slant threshold triggered; 2 = HET 2 A end stopping particles low-gain mode; 3 = HET 2 B end stopping particles low-gain mode. Units of E_{\min} and E_{\max} are MeV nuc $^{-1}$. Points in figures are plotted at $(E_{\min} + E_{\max})/2$. Units of intensity J are (m 2 s sr MeV nuc $^{-1}$) $^{-1}$.

Table 10
Voyager 1 Intensities of Electrons for 2012/342–2015/181

Name	Corrected Rate (c s $^{-1}$)	unc	Bkg %	E_{\min} (MeV)	E_{\max} (MeV)	E_{plot} (MeV)	J (m 2 s sr MeV) $^{-1}$	sig	Tel Type
ch01	1.24e–01	1.25e–02	15	2.7	4.4	3.5	1.01e+03	1.01e+02	1
ch23	1.44e–01	1.44e–02	11	3.8	5.8	4.7	7.11e+02	7.12e+01	1
ch45	1.04e–01	1.05e–02	10	5.6	8.5	6.9	3.98e+02	3.99e+01	1
ch67	4.43e–02	4.44e–03	10	8.0	12.9	10.2	2.02e+02	2.03e+01	1
ch89	1.91e–02	1.92e–03	9	10.0	14.2	11.9	1.79e+02	1.80e+01	1
D13	1.89e–01	1.89e–02	2.1	5.3	13.2	8.4	3.54e+02	3.54e+01	2
D14	7.30e–02	7.30e–03	4.1	9.5	25.1	15.4	1.52e+02	1.52e+01	2
D15	3.13e–02	3.13e–03	8.6	15.0	44.6	25.9	7.60e+01	7.61e+00	2
D16	1.40e–02	1.40e–03	16.9	21.0	74.1	39.5	4.18e+01	4.18e+00	2

Note. The column labeled “unc” contains the uncertainties on the rates corrected for background, which have a 10% systematic uncertainty added in quadrature to the statistical uncertainties. The energy range corresponding to the intensity, J, is $E_{\min} – E_{\max}$. E_{plot} denotes the energy of the plotted points. The column labeled “sig” refers to the 1σ uncertainties on J, which are formed by scaling the “unc” values. The Tel Type numbers denote from which telescope and mode the data are derived: 1 = HET 2 B stopping electron mode and 2 = TET (Stone et al. 1977).

Table 11
Propagation Model Parameters

Parameter	DR	PD1	PD2
D_0 (10 28 cm 2 s $^{-1}$) ^a	14.60 ± 0.20	12.20 ± 0.46	12.3 ± 1.6
δ_1	0.3268 ± 0.0051	−0.631 ± 0.023	−0.641 ± 0.042
δ_2	...	0.570 ± 0.022	0.578 ± 0.073
ρ_d (GV)	...	4.886 ± 0.060	4.84 ± 0.10
v_A (km s $^{-1}$)	42.20 ± 0.61
z_h (kpc)	4	4	4
r_h (kpc)	25	25	25
χ^2	394.3	437.1	400.4

Note.

^a Normalization at 10 GV.

as LETs A, B, C, and D; two double-ended high-energy telescopes (HETs), referred to as HET 1A, HET 1B, HET 2A, and HET 2B; and an electron telescope (TET). Because the silicon detector stack is significantly thicker in the HET B stopping analysis mode, the B end yields the highest-energy spectral points for particles that stop within the detectors of any telescope, while providing some overlap in energy coverage with the A end. There is also a penetrating mode for each HET telescope that provides even higher-energy spectral points. In addition there are two gain states on HET and a pair of so-called “slant thresholds,” which typically provide for separate telemetry buffers for the more abundant lower-Z nuclei versus the rarer higher-Z nuclei, so that telemetry is not dominated by lower-Z particles. There is also an electron mode in HET that

uses a slant threshold as well. The LETs have only one gain state but they do have slant thresholds for the same reasons as HET does, except LET does not have an electron mode.

There are several types of analysis to consider and the effort of producing energy spectra from each type has been divided up among the investigators and their institutions as follows. The initial formatting of the raw data obtained from the Deep Space Network is done at the Jet Propulsion Laboratory for all instrument teams on *Voyager*. The CRS data is transferred to *Voyager* CRS team members at the Goddard Space Flight Center (GSFC), where initial analysis takes place.

Data products are delivered to Caltech, where the analysis of LET and HET AS (A Stopping) data is done. This analysis covers the lower-energy portions of nuclei with Z = 1 through 28. A part of the HET AS analysis is a GEANT4 simulation (Agostinelli et al. 2003; Allison et al. 2006) done at GSFC. Data products are also delivered to New Mexico State University (NMSU), where the analysis of HET BS (B Stopping) low-gain data takes place.

The electron analysis is a joint effort of Caltech, GSFC, and NMSU, with GSFC providing the background-corrected counting rates in four energy ranges of TET and in five paired pulse-height analysis channels from the HET B stopping electron mode. GSFC also supplies the GEANT4-derived response functions for both HET and TET. Caltech takes the final step of deriving the energy spectra.

The techniques used to derive energy spectra often differ somewhat among the institutions. For HET AS and HET BS, this yields a sense of the systematic uncertainties, since there is some overlap in the energy coverage. These different techniques are described below.

Table 12
Injection Model Parameters and Modulation Potentials

CR Species	Parameter	DR	PD1	PD2
p ($Z = 1$)	γ_0	-0.6 ± 3.7	1.183 ± 0.025	1.186 ± 0.024
	γ_1	1.935 ± 0.011	2.945 ± 0.021	2.947 ± 0.024
	γ_2	2.4742 ± 0.0090	2.2283 ± 0.0042	2.2225 ± 0.0061
	$\rho_{q,1}$ (GV)	0.117 ± 0.028	1.251 ± 0.031	1.244 ± 0.031
	$\rho_{q,2}$ (GV)	18.0 ± 1.8	6.62 ± 0.15	6.50 ± 0.18
	X_p at 10 GV ^a	2.41×10^4	2.48×10^4	2.53×10^4
	N_p ($10^{-3} \text{ cm}^{-2} \text{ sr}^{-1} \text{ s}^{-1} \text{ GeV}^{-1}$) at 10 GeV	2.363 ± 0.010	2.2739 ± 0.0043	2.2818 ± 0.0043
	γ_0	0.9 ± 2.5	1.507 ± 0.021	1.514 ± 0.022
	γ_1	1.9667 ± 0.0051	3.018 ± 0.068	3.02 ± 0.15
	γ_2	2.4432 ± 0.0085	2.2431 ± 0.0052	2.2356 ± 0.0042
He ($Z = 2$)	$\rho_{q,1}$ (GV)	0.26 ± 0.10	2.457 ± 0.045	2.457 ± 0.073
	$\rho_{q,2}$ (GV)	21.7850 ± 0.0044	4.51 ± 0.15	4.49 ± 0.21
	X_{He} at 10 GV ^a	8463 ± 52	1.02×10^4	1.03×10^4
	Φ_{PAMELA} (MV)	472.1 ± 6.8	468.5 ± 8.4	467.6 ± 9.9
	$\chi^2(Z \leq 2)$	522.9	614.8	602.3
	γ_0	1.338 ± 0.024	1.329 ± 0.031	0.88 ± 0.16
	γ_1	2.2076 ± 0.0085	2.349 ± 0.015	1.63 ± 0.16
	γ_2	2.657 ± 0.032	...	2.3266 ± 0.0025
	$\rho_{q,1}$ (GV)	2.017 ± 0.027	2.047 ± 0.038	0.8666 ± 0.0019
	$\rho_{q,2}$ (GV)	18.62 ± 0.50	...	2.28 ± 0.41
$Z > 2$	$\Phi_{\text{HEAO-3}}$ (MV)	889 ± 11	785 ± 15	755 ± 62
	$\Phi_{\text{ACE-CRIS}}$ (MV)	520.0 ± 5.1	485.1 ± 7.0	453 ± 23

Note.

^a Relative to Si, $X_{\text{Si}} = 100$, see Equation (14).

Table 13
GALPROP Model DR Intensities in LISM for H through N

E , MeV nuc $^{-1}$	Intensities in (m 2 s sr MeV nuc $^{-1}$) $^{-1}$						
	H	He	Li	Be	B	C	N
3.00e+00	1.40e+01	1.16e+00	2.51e-04	9.48e-05	3.84e-04	1.08e-02	1.13e-03
3.60e+00	1.80e+01	1.41e+00	3.05e-04	1.15e-04	4.64e-04	1.23e-02	1.30e-03
4.32e+00	2.01e+01	1.54e+00	3.46e-04	1.32e-04	5.38e-04	1.35e-02	1.46e-03
5.18e+00	2.16e+01	1.66e+00	3.89e-04	1.52e-04	6.22e-04	1.48e-02	1.63e-03
6.22e+00	2.29e+01	1.77e+00	4.40e-04	1.75e-04	7.21e-04	1.62e-02	1.82e-03
...

Note. The energy range extends to 1.07×10^9 MeV nuc $^{-1}$ and the element range extends through Ni.

(This table is available in its entirety in machine-readable form.)

Table 14
GALPROP Model PD1 Intensities in LISM for H through N

E , MeV nuc $^{-1}$	Intensities in (m 2 s sr MeV nuc $^{-1}$) $^{-1}$						
	H	He	Li	Be	B	C	N
3.00e+00	2.12e+01	1.39e+00	3.53e-04	8.61e-05	3.66e-04	1.24e-02	1.29e-03
3.60e+00	2.20e+01	1.48e+00	3.88e-04	9.85e-05	4.23e-04	1.36e-02	1.44e-03
4.32e+00	2.29e+01	1.57e+00	4.29e-04	1.13e-04	4.89e-04	1.49e-02	1.59e-03
5.18e+00	2.37e+01	1.65e+00	4.75e-04	1.30e-04	5.67e-04	1.62e-02	1.77e-03
6.22e+00	2.45e+01	1.74e+00	5.28e-04	1.50e-04	6.59e-04	1.77e-02	1.96e-03
...

Note. The energy range extends to 1.07×10^9 MeV nuc $^{-1}$ and the element range extends through Ni.

(This table is available in its entirety in machine-readable form.)

Table 15
GALPROP Model PD2 Intensities in LISIM for H Through N

E , MeV nuc $^{-1}$	Intensities in (m 2 s sr MeV nuc $^{-1}$) $^{-1}$						
	H	He	Li	Be	B	C	N
3.00e+00	2.12e+01	1.40e+00	2.87e-04	8.91e-05	3.78e-04	9.48e-03	1.07e-03
3.60e+00	2.20e+01	1.48e+00	3.22e-04	1.02e-04	4.37e-04	1.06e-02	1.20e-03
4.32e+00	2.29e+01	1.57e+00	3.61e-04	1.17e-04	5.05e-04	1.18e-02	1.36e-03
5.18e+00	2.37e+01	1.66e+00	4.07e-04	1.34e-04	5.86e-04	1.32e-02	1.54e-03
6.22e+00	2.44e+01	1.75e+00	4.61e-04	1.55e-04	6.81e-04	1.47e-02	1.74e-03
...

Note. The energy range extends to 1.07×10^9 MeV nuc $^{-1}$ and the element range extends through Ni.
(This table is available in its entirety in machine-readable form.)

Table 16
LBM Intensities in LISIM for H through O

E , MeV nuc $^{-1}$	Intensities in (m 2 s sr MeV nuc $^{-1}$) $^{-1}$						
	H	He	Be	B	C	N	O
3.00e+00	2.15e+01	1.90e+00	2.46e-05	1.82e-04	1.98e-02	1.31e-03	1.81e-02
4.00e+00	2.39e+01	2.12e+00	3.81e-05	2.60e-04	2.39e-02	1.62e-03	2.21e-02
6.00e+00	2.62e+01	2.31e+00	5.84e-05	3.71e-04	2.80e-02	1.95e-03	2.63e-02
8.00e+00	2.80e+01	2.47e+00	8.92e-05	5.27e-04	3.18e-02	2.30e-03	3.06e-02
1.00e+01	2.96e+01	2.60e+00	1.36e-04	7.50e-04	3.55e-02	2.69e-03	3.45e-02
...

Note. The energy range extends to 1.35×10^5 MeV nuc $^{-1}$ and the element range extends through Ni, with the exception of Li and Ca.
(This table is available in its entirety in machine-readable form.)

A.1. LET and HET A Stopping

The LET and HET A stopping analyses generally follow the techniques outlined for LET in Cook (1981) and Cook et al. (1984). Both HET and LET are composed of a stack of cylindrical, solid-state detectors, the first two of which are thinner than the subsequent detectors and spaced apart from each other in order to establish a field of view. Three energy losses are recorded for each incident particle, one each from the first two detectors and the third represents the sum of the energy lost in the remaining detectors (one in the case of LET), except for the last detector, which is used in anti-coincidence to identify and eliminate penetrating particles.

As described in Cook (1981) and Cook et al. (1984), these three energy losses allow for two semi-independent determinations of the nuclear Z of the particle to be determined, provided the particle penetrates the first two detectors, as is the case in the analysis presented here. A consistency criterion is applied to these two determinations of Z to eliminate background events, and the average of the two Z determinations gives the estimated Z of the particle, which is generally not an integer. Using a model of the telescope, including the thickness of any window and/or thermal blanket material covering the entrance aperture and any inactive thickness of the detectors, incident energy per nucleon bins are mapped to energy-loss bins in the active thicknesses of the detectors.

In the analysis used in this paper, only LET C and D and HET 2 are used, due to a “block I” problem in the electronics affecting LETs A and B and HET 1, which occurred on 2/8/82 on *Voyager 1*. Although the problem that occurred does not prevent the block I data from being analyzed, it effectively does prevent the charge-consistency criterion from being applied. As a result, we did not use LETs A and B and HET 1 in this analysis.

In the case of the analysis of $Z > 2$ nuclei in the HET AS low-gain mode, one new addition to the analysis procedure beyond that described in Cook (1981) and Cook et al. (1984) is the use of a GEANT4 simulation. A model of the telescope is subjected in simulation to an isotropic intensity of the dominant isotope of each nucleus from B through Ni. The simulations use a flat energy spectrum with enough energy range to cover the response of the telescope. The idea is to account for losses due to nuclear interactions and mis-identifications due to such interactions or due to energy losses in dead layers of the detectors that are not recorded. In addition, any errors in the geometrical factor used in the initial determination of the intensities from the observations are corrected as a result of the procedure described below.

Each simulation results in counts being observed in one or more energy-bin-Z combinations. The contributions from the 24 simulations, one for each Z from $Z = 5$ to $Z = 28$, to a given energy bin for a given Z are summed and compared with the observed counts. Then, each energy-bin-Z combination from the simulation is assigned a variable intensity factor, and the factors are adjusted until the observed counts and the simulated counts match in a least-squares sense. This procedure determines the best-fit intensity factors, which are then applied to the simulated intensities to derive the reported intensities for each energy-bin-Z combination. The uncertainties are derived from the best-fit counts in each energy-bin-Z combination.

A.2. HET Penetrating H and He

The penetrating data set (PEN mode) consists of particles that trigger detectors B1, B2, and C1 (see Stone et al. (1977) for detector terminology). Three pulse heights (PHs) are returned for each event in the form of channel numbers, which are approximately linearly related to the energy losses in the

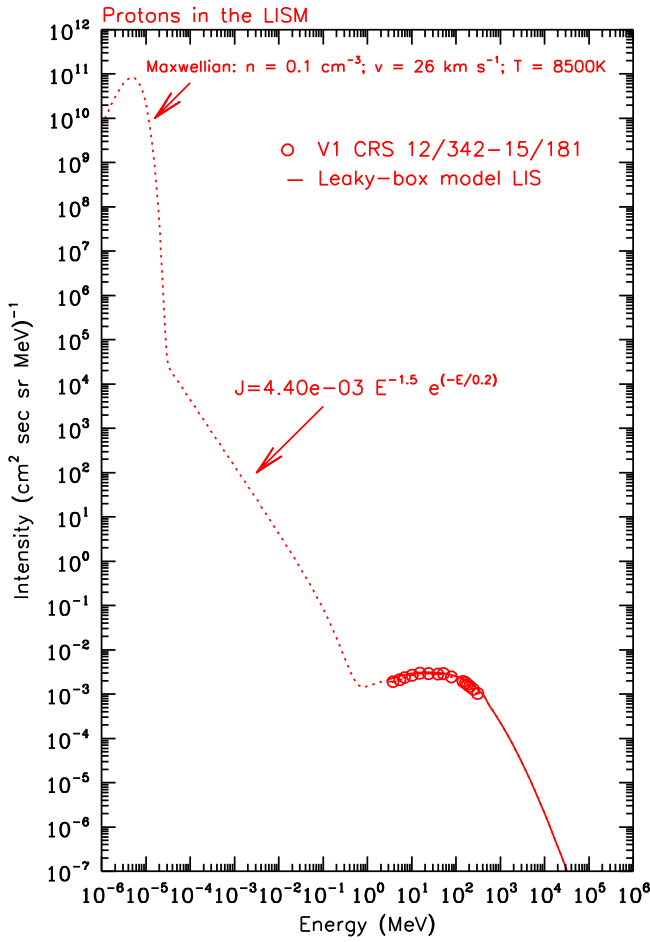


Figure 16. Possible suprathermal tail on interstellar wind distribution that could account for factor of 12 increase in ionization rate of atomic H. The portion of the GCR LISM spectrum ≥ 3 MeV is from the LBM model.

detectors. These PHs are from $B1$, $C1$, and $C4+C3+C2$, which we refer to here as $C432$. For each $C432$ channel applicable to the species (proton or helium nucleus), a response table contains limits of $B1$ channels, limits of $C1$ channels, and the highest incident energy that triggers this $C432$ channel. If the $B1$ and $C1$ PHs of an event fall within the $B1$ and $C1$ limits, respectively, for the $C432$ channel of a certain element, then this event is identified as belonging to that element, and its incident energy lies between the incident energy corresponding to the next lower $C432$ channel and that corresponding to $C432$ of the event.

The construction of the response table proceeds as follows. For the applicable range of incident energies, energy losses along a mean trajectory through the telescope are computed using a range-energy relation. From these energy losses, mean energy losses in $B1$ and $C1$ for $C432$ energy losses corresponding to the $C432$ channel boundaries are located. Representative samples of flight data are examined to estimate the spread of $B1$ and $C1$ PHs about the mean values. These estimates are used to compute the limits on $B1$ and $C1$ for each $C432$ channel for each element.

The effect of nuclear interactions is accounted for in an approximate way. First, for protons it is assumed that the effect of interactions is negligible. For He, it is assumed there is an 11% reduction in He intensities due to nuclear interactions and

that correction is accounted for by using different geometry factors for H as compared to He.

A.3. HET B Stopping $Z > 2$

The time period for this type of analysis of nuclei uses a slightly shorter period, 2012/342–2014/365, which is equivalent to the longer period since we have found no evidence of a radial gradient. This analysis involves three parameters: $B1$, $B2$, and $C432$ ($C4+C3+C2$). Matrices are made of each combination of variables and the energy scale of the PH is determined for the most abundant charges, and the coordinates of the consistency line in $B1$ versus $B2$ are also determined. A simple consistency criteria, $1.33 < B1/B2 < 2.20$, is then applied. The resulting charge matrix, $C432$ versus $B1+B2$, is essentially background free, e.g., Li, ^7Be , ^9Be , F, and P are resolved visually with no background.

The energy scale for each charge is determined by comparing the maximum stopping PH channel with the calculated maximum energy loss, E_{\max} . These scales are adjusted so that the maximum PH/E_{\max} loss is within 1% for all major charges. The energy scale is then defined as the energy that is equal to the energy loss that is calculated for $\text{PH} = 0.77$, 0.54 , 0.333 , and $0.166 \times$ the maximum PH for each charge. In effect, the energy scale for each charge is divided into four intervals between E_{\max} and the energy corresponding to a $\text{PH} = 0.166 \times$ maximum PH.

Correction factors for losses due to nuclear interactions are calculated and vary from 1.028 to 1.069 for the four energy intervals of Li to factors of 1.06–1.18 for the four energy intervals of Fe.

A.4. Electrons

The TET and HET BSe (B stopping electron) modes are described in Stone et al. (1977). We first discuss the analysis of data from the TET telescope. TET consists of a set of eight cylindrical, 3 mm thick, silicon solid-state detectors, and a set of interleaved absorbers made of a tungsten alloy (Mallory 2000 = 90% W, 5% Cu, and 5% Ni; density = 18 g cm^{-3}). PHs are captured for the front two detectors, referred to as D1 and D2. These detectors have both a lower (~ 500 keV) and an upper (~ 2.5 MeV) threshold. An electron event is identified as one that triggers the lower threshold of D1 and D2 in coincidence but not their upper threshold and also triggers the threshold for D3 and possibly triggers the thresholds of detectors deeper in the stack. For the analysis employed here, average counting rates were gathered over the time period 2012/342–2015/181 for particles that satisfy in coincidence the threshold requirements for D1, D2, and D3 (D13); D1, D2, D3, and D4 (D14); D1, D2, D3, D4, and D5 (D15); and D1, D2, D3, D4, D5, and D6 (D16). Response functions for each of these “range rates” were determined from a GEANT4 simulation. These response functions, $F(E)$, in units of $\text{m}^2 \text{ sr}$ are shown in the top panel of Figure 17. Given a trial energy spectrum incident isotropically on TET, rates for D13, D14, D15, and D16 can be calculated by integrating the product of the response function and the energy spectrum over a broad energy range:

$$R = \int_{E_{\text{low}}}^{E_{\text{high}}} J(E)F(E)dE. \quad (7)$$

These rates can then be compared to observed, background-corrected rates.

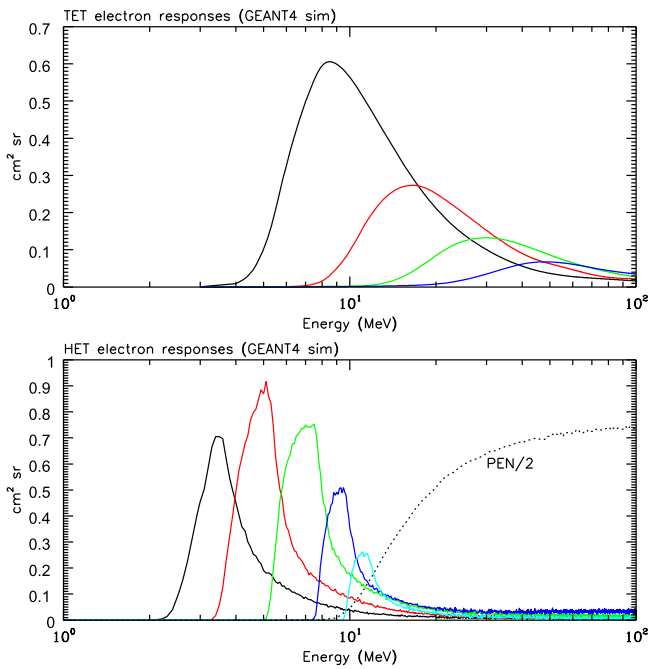


Figure 17. GEANT4-derived response functions for rates of four TET ranges and five HET channel pairs, as described in the text. In addition, the response of HET to electrons that penetrate the HET telescope is shown as the dotted line, which is used in calculating the electron contribution to the PENH rate shown in Figure 1.

The upper threshold on the D1 and D2 detectors serves to reject most protons and other nuclei, but very high-energy protons can satisfy the trigger criteria and mimic the signature of an electron, e.g., if the proton were to interact and stop in an absorber. Each detector has an annular “guard” ring incorporated into the detector design, which limits to some extent particle entry from the sides of the telescope. However, since the detector spacing has to accommodate the interleaved absorbers, protons, e.g., can enter through the gaps, interact in an absorber, and send an interaction product up through the entrance aperture, potentially causing a background event.

The background arises principally from high-energy protons, and for much of the *Voyager* mission it dominated the telescope response. We have correlated the observed D13, D14, D15, and D16 rates with a rate of protons with 220–646 MeV from 1992 to 2002.2, when it appears the observed rate is all background, and used that correlation to estimate the background after \sim 2005 when the rates began to show a response to real electrons. In Figure 18 we show the results of that background analysis procedure for D13 and D16, the rates showing the least and most background, respectively.

The HET BSe analysis is very similar, except in this case there are no absorbers in the telescope and we do not use “range rates.” In the BSe mode, PHs are returned from detectors *B1*, *B2*, and *C4+C3+C2* (*C432*). To reject background, we use the following consistency criteria in *B1* and *B2*: $(B1 + B2) < 16$ and $(-6.0 + 0.92 B2) \leq B1 < (4.5 + 0.92 B2)$. Using these criteria we obtain background-corrected rates in the low channels of *C432*. We form five rates, combining in pairs channels 0 and 1 (*ch01*), channels 2 and 3, (*ch23*), etc. We use GEANT4 simulations of the HET telescope to calculate response functions for these channel pairs, which are shown in the bottom panel of Figure 17.

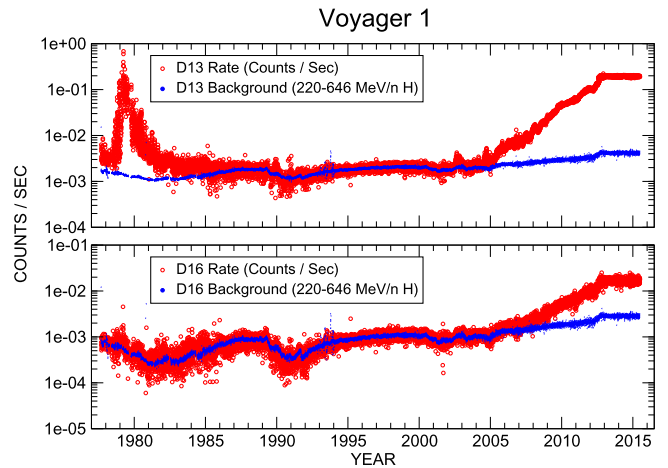


Figure 18. Daily averaged D13 (top) and D16 (bottom) counting rates since launch in 1977. Also shown is the estimated rate of background events.

The result of this procedure is to obtain nine background-corrected rates, four from TET and five from the HET 2 B stopping electron mode, and we compare these rates with those calculated from a trial LISM electron energy spectrum. We use a power-law form for a trial energy spectrum, $J = A (E/10)^b$, where E is in MeV and the two free parameters, A and b , are varied until a best-fit is achieved to the observed, background-corrected rates. In this process, a 10% systematic uncertainty was added in quadrature to the statistical uncertainty of each rate.

To determine the energy limits corresponding to each rate, we examine the integrand of Equation (7) and determine the horizontal line displaced down from the peak that captures 68% of the distribution. Where the horizontal line intersects the distribution below and above the peak are designated the minimum and maximum energies for that rate, respectively.

The result of the procedure described above is a power law that represents the energy spectrum that results in the best fit to the background-corrected rates. To help visualize the data that went into determining that power-law, we assign an intensity to each rate, which is formed from the value on the power-law at the E_{plot} in Table 10 multiplied by the ratio of the best-fit rate to the background-corrected rate. The TET and BSe intensities are shown in Table 10 and in Figure 8.

APPENDIX B MODELS

B.1. Leaky-box Model

This program was originally written by the French (Engelmann et al. 1990) and was used in cross-section studies with H targets at the SACLAY accelerator in the 1990s. The latest publication using a slightly modified version of this program is Webber & Higbie (2009), where its predictions of the interstellar H and He spectra were consistent with the *V1* observations down to \sim 100 MeV nuc $^{-1}$. The modification was to use source spectra that are power laws in rigidity rather than power laws in momentum per nucleon, which were used in Engelmann et al. (1990). The intensities calculated for this paper are tuned to match the observed *V1* intensities at 100 MeV nuc $^{-1}$ for only the six basic primary nuclei: C, O, Ne, Mg, Si, and Fe. These spectra are then matched to the available

high-energy data for these nuclei and also H and He above 10 GeV nuc^{-1} .

The first step in the overall process of matching at higher energies was to determine the interstellar diffusion coefficient from new B/C ratio measurements by AMS-2⁷ from ~ 1 to nearly $1000 \text{ GeV nuc}^{-1}$. This results in a diffusion coefficient which is $\sim \rho^{0.47}$ above $\rho_0 = 1 \text{ GV}$, where ρ is rigidity. Below this lower limit, which may be varied, the diffusion coefficient dependence on rigidity is assumed to change by one power to be $\rho^{-0.53}$ at lower rigidities.

This rigidity dependence determines, in a leaky-box model, that the path length will be $\lambda = 22.3\beta\rho^{-0.47} \text{ g cm}^{-2}$ above a value of ρ_0 . Below $\rho_0 = 1.0 \text{ GV}$, $\lambda = 33.7\beta^{3/2} \text{ g cm}^{-2}$. This path length will be between $\sim 4 \text{ g cm}^{-2}$ at $\sim 10 \text{ MeV nuc}^{-1}$ and $\sim 10 \text{ g cm}^{-2}$ at 120 MeV nuc^{-1} ($\rho = 1.0$). The intensities shown for the LBM in the figures are calculated using this path length, which has an exponential path length distribution at all path lengths. This diffusion coefficient, along with an assumed injection spectrum $\sim \rho^{-2.26}$, leads to spectra $\sim \rho^{-2.73}$ at high rigidities, which match those that are observed.

Tuning the results of the LBM to fit the individual primary and secondary spectra below $\sim 100 \text{ MeV nuc}^{-1}$ involves several factors such as the path length, the path length distribution, and the source composition as in a nested LBM model, for example. This is best done, we believe, by studying and comparing features of the individual spectra of primary and secondary model which we are starting to do now. So in general our fits may not be as good at the lower energies.

Table 16 shows the LISM intensities of all nuclei species for the LBM model, except for Li and Ca, which were not calculated, over the energy range $3\text{--}134943 \text{ MeV nuc}^{-1}$. For the purposes of accounting for the PENH rate and for calculating the energy density of cosmic rays and the ionization rate of atomic H, the LBM LISM energy spectra were extrapolated to $1 \times 10^7 \text{ MeV nuc}^{-1}$ using power laws with index -2.7 .

The elemental source abundances are shown in Table 5 together with those from GALPROP models.

B.2. GALPROP models

The GALPROP project began in late 1990s (Moskalenko & Strong 1998; Strong & Moskalenko 1998) and has been in continuous development since. The code is available from the dedicated web site⁸ where a facility for users to run the code via online forms in a web browser is also provided (Vladimirov et al. 2011).

The GALPROP model calculates cosmic-ray propagation in the Galaxy and associated diffuse emissions (Strong et al. 2007). The GALPROP code solves the GCR transport equation for a given source distribution and boundary conditions for all GCR species. This equation includes diffusion, a Galactic wind (convection), diffusive reacceleration in the ISM, energy losses, nuclear fragmentation, radioactive decay, and production of secondary particles and

isotopes:

$$\frac{\partial \psi}{\partial t} = q(\mathbf{r}, p) + \nabla \cdot (D_{xx} \nabla \psi - \mathbf{V} \psi) + \frac{\partial}{\partial p} p^2 D_{pp} \frac{\partial}{\partial p} \frac{1}{p^2} \psi - \frac{\partial}{\partial p} \left[\dot{p} \psi - \frac{p}{3} (\nabla \cdot \mathbf{V}) \psi \right] - \frac{1}{\tau_f} \psi - \frac{1}{\tau_r} \psi, \quad (8)$$

where $\psi = \psi(\mathbf{r}, p, t)$ is the GCR number density per unit total particle momentum, i.e., $\psi(p)dp = 4\pi p^2 f(p)dp$ in terms of phase-space density $f(p)$, p is the total particle momentum, \mathbf{r} is the position in space, $q(\mathbf{r}, p)$ is the source term, D_{xx} is the spatial diffusion coefficient, \mathbf{V} is the convection velocity, reacceleration is described as diffusion in momentum space with diffusion coefficient D_{pp} , $\dot{p} \equiv dp/dt$ is the momentum loss rate, τ_f is the timescale for fragmentation, and τ_r is the timescale for radioactive decay. The numerical solution of the transport equation is based on a Crank–Nicholson (Press et al. 1992) implicit second-order scheme. The spatial boundary conditions assume free particle escape, i.e., $\psi(r_h, z, p) = \psi(r, \pm z_h, p) = 0$, where r_h and z_h are the boundaries for a cylindrically symmetric geometry.

The source function $q(\mathbf{r}, p)$ is a sum of two terms:

$$q(\mathbf{r}, p) = q'(\mathbf{r}, p) + q_f''(\mathbf{r}, p), \quad (9)$$

where $q'(\mathbf{r}, p) = q'(\mathbf{r})q'(\rho)$ represents the primary sources of GCRs, such as supernova remnants (SNRs), and the q_f'' describes the secondary production due to the fragmentation of heavier CR nuclei in the ISM, $\rho \equiv \text{pc}/\text{Ze}$ is the magnetic rigidity, and Ze is the nucleus charge.

The spatial distribution of GCR sources is based on the distribution of pulsars and SNRs in the Galaxy (e.g., Case & Bhattacharya 1998; Lorimer et al. 2006). Their radial distribution is parameterized with

$$q'(r) \propto (r/r_\odot)^\alpha \exp\left(-\beta \frac{r - r_\odot}{r_\odot}\right), \quad (10)$$

where $r_\odot = 8.5 \text{ kpc}$, $\alpha = 1.25$ and $\beta = 3.56$. The distribution has a cut off at 15 kpc . We assume an exponential dependence with distance z above the plane with a scale height of 200 pc .

The energy dependence of the GCR source spectrum, i.e., the injection spectrum of primary nuclei, can be arbitrary, but here we use a broken power law in particle rigidity:

$$q'(\rho) \propto \begin{cases} (\rho/\rho_{q,1})^{-\gamma_0}, & \rho \leq \rho_{q,1} \\ (\rho/\rho_{q,1})^{-\gamma_1}, & \rho_{q,1} < \rho \leq \rho_{q,2} \\ (\rho/\rho_{q,2})^{-\gamma_2} (\rho_{q,2}/\rho_{q,1})^{-\gamma_1}, & \rho \geq \rho_{q,2} \end{cases} \quad (11)$$

where $\rho_{q,i}$ are the positions of the breaks ($i = 1, 2$), and γ_j is the spectral index ($j = 0, 1, 2$).

The spatial diffusion coefficient is given by

$$D_{xx}(\rho) \propto \beta(\rho/\rho_d)^\delta, \quad \delta = \begin{cases} \delta_1 & \text{for } \rho < \rho_d \\ \delta_2 & \text{for } \rho \geq \rho_d \end{cases} \quad (12)$$

$$D_{xx}(\rho_0) = D_0, \quad \rho_0 = 10 \text{ GV},$$

where ρ_d is the rigidity of the break, ρ_0 is the normalization rigidity, and $\beta \equiv v/c$.

Note that even though a spatially varying diffusion coefficient option is available in the GALPROP code, we do

⁷ Preliminary results as shown at the “AMS-02 Days at CERN”: <https://indico.cern.ch/event/381134/timetable/#20150415>.

⁸ <http://galprop.stanford.edu>

not use it here. Such choice is motivated by the desire to avoid too many unconstrained parameters and to keep the model as simple as possible while it is still able to reproduce the available data (Occam's razor argument).

The details of physical processes and data used in the GALPROP code, as well as the numerical scheme, can be found elsewhere (Strong et al. 2007, and references therein). A list of relevant publications is available in Vladimirov et al. (2011); the aforementioned GALPROP web site contains additional information and publications.

B.3. Diffusive-reacceleration and Plain Diffusion Models

We explore two basic types of propagation models that are widely used to reproduce GCR data: the *diffusive-reacceleration* (DR) model and the *plain diffusion* (PD) model. These models have been used in a number of studies utilizing the GALPROP code (e.g., Moskalenko et al. 2002; Ptuskin et al. 2006; Trotta et al. 2011; Ackermann et al. 2012; Jóhannesson et al. 2016, and references therein).

The DR model assumes that low-energy GCRs in the ISM participate in the second-order Fermi acceleration process. This process is caused by stochastic interactions of GCR particles with moving magnetic turbulences. Averaged over time, such interactions can be described as diffusion in the momentum space with a diffusion coefficient D_{pp} , which results in energy gain for low-energy particles.

The spatial diffusion coefficient D_{xx} and D_{pp} are related through (Berezinskii et al. 1990; Seo & Ptuskin 1994)

$$D_{pp}D_{xx} = \frac{4p^2 v_{\text{Alf}}^2}{3\delta(4 - \delta^2)(4 - \delta)w}, \quad (13)$$

where w characterizes the level of turbulence (we take $w = 1$ because only the quantity v_{Alf}^2/w is relevant), and $\delta = 1/3$ for a Kolmogorov spectrum of interstellar turbulence (Kolmogorov 1941) or $\delta = 1/2$ for an Iroshnikov–Kraichnan cascade (Iroshnikov 1964; Kraichnan 1965), but can also be arbitrary. Matching the B/C ratio below 1 GeV nuc⁻¹ in diffusive reacceleration models requires large values of v_{Alf} , of the order of some ten km s⁻¹. If the injection spectrum is a single power-law, strong reacceleration is known to produce a large bump in the proton spectrum at low energies. In order to avoid it, the DR model requires a flattening of the injection spectrum at low energies. The simplest solution is to introduce a break in the GCR injection spectrum around $\rho \sim 10$ GV.

The PD model assumes no reacceleration process, $v_{\text{Alf}} = 0$. However, in order to fit the B/C data below 1 GeV nuc⁻¹, the PD model requires a low-energy break in the diffusion coefficient D_{xx} . Specifically, the diffusion coefficient in the PD model must decrease as the energy increases up to ~ 4 GV in order to fit the B/C measurements below 1 GeV nuc⁻¹. A possible physical justification of such behavior of $D_{xx}(\rho)$ is given by Ptuskin et al. (2006) and involves damping of interstellar turbulence due to the interactions with low-energy CRs.

B.4. Model Tuning

The model tuning was performed in an iterative fashion using the Minuit2 package from ROOT⁹ by minimizing the χ^2 . The halo size was fixed to $r_h = 25$ kpc, $z_h = 4$ kpc in agreement

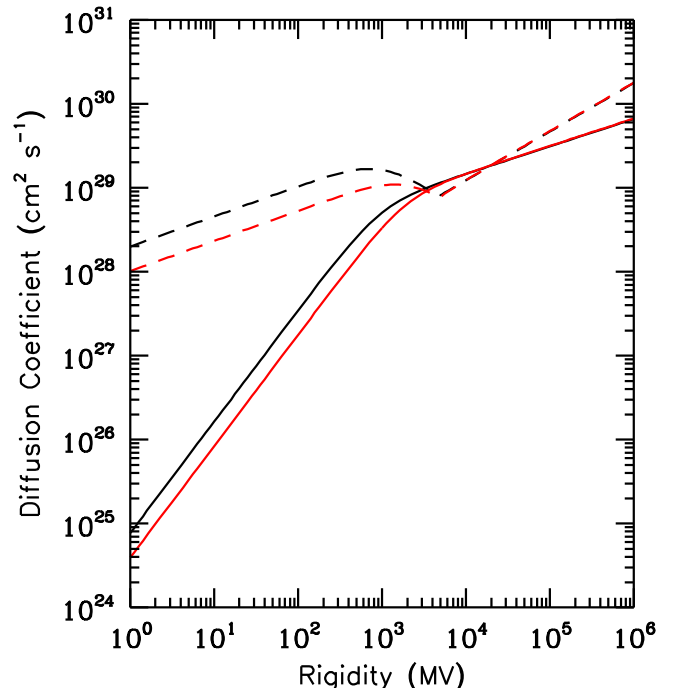


Figure 19. Rigidity dependence of the diffusion coefficients for the GALPROP models. Shown are curves for the DR model (solid) and for the PD2 model (dashed). The curve for the PD1 model is almost identical to that for PD2. We show curves for two values of atomic number over charge, $A/Z = 1$ (black), 2 (red).

with the results from Trotta et al. (2011). In the first step, we tune the propagation parameters, the injection spectra, and abundances for the most abundant elements ($Z = 6$ –14): C, N, O, Ne, Mg, and Si, as well as the B/C ratio, as described below. The models were tuned to data from VI, ACE-CRIS (George et al. 2009), HEAO-3 (Engelmann et al. 1990), and CREAM (Yoon et al. 2011). The ACE-CRIS and HEAO-3 data were corrected for solar modulation using a force-field approximation (Gleeson & Axford 1968) with a free modulation potential Φ for each experiment. Note that using more recent ACE-CRIS data (Lave et al. 2013) yields a different modulation potential, but does not change our results thus providing a good test for the employed procedure.

The spectral shape of the injection spectrum was assumed to be the same for all elements $Z > 2$, but the isotopic abundance of individual isotopes is left free. To speed up the fitting procedure at this stage, we tune only the most abundant isotopes, such as ^{12}C , ^{14}N , ^{16}O , ^{20}Ne , ^{24}Mg , and ^{28}Si . Other isotopes were kept fixed at preliminary values from the abundances fits (Moskalenko et al. 2008). The isotopic abundance is defined as the ratio (Table 5)

$$X_Z = 100 \frac{q'_Z(\rho_0)}{q'_{\text{Si}}(\rho_0)}, \quad (14)$$

where $q'_Z(\rho)$ is the injection spectrum given by Equation (11), and $\rho_0 = 10$ GV. The exact rigidity ρ_0 has no effect on the injection abundances when the spectral shape is the same for all species ($Z > 2$). Once the propagation parameters are optimized, *all* isotopic abundances are fitted to the ACE-CRIS data. At the end of the procedure, the propagation parameters are refitted with the new isotopic abundances. After this step the

⁹ <http://root.cern.ch>

propagation parameters, the injection spectrum for $Z > 2$ nuclei, and their isotopic abundances are fixed.

The resulting parameters from the model tuning are given in Tables 11 and 12. Both types of models that we use, DR and PD, require breaks in the injection spectrum to match the GCR data. Two breaks are required for the DR model. In case of the PD model, we use one break (PD1 model, $\rho_{q,2} = \infty$) and two breaks (PD2 model). We note that the DR model is statistically favored with high significance, while the PD1 model is least favored. The additional low-energy break in the injection spectra (PD2 model) is, therefore, significant from the viewpoint of the goodness of the fit. However, the diffusion parameters are nearly identical for the PD1 and PD2 models and are not affected by the low-energy injection. Figure 19 shows the rigidity dependence of the diffusion coefficient for all three models. The upturn at low energies in both PD models is very similar to the effect of wave damping (Ptuskin et al. 2006).

The p and He injection spectra are adjusted separately. The injection spectrum for those elements required two breaks for all models to fully match the data. This time the models are tuned to data from VI and PAMELA (Adriani et al. 2011) using the force-field approximation to account for the solar modulation in the PAMELA data. At the end of the run, the flux of observed protons at the kinetic energy $E_{k,0} = 10 \text{ GeV nuc}^{-1}$ is normalized to N_p . The final parameters from the p and He fits are shown in Table 12.

Not surprisingly, the results for the two PD models are very close, but not identical due to a small difference in the propagation parameters (Table 11). Again the DR model is statistically favored. The He injection spectrum is harder than that of protons at higher energies for all models, while the spectra of heavier elements are softer than that of both protons and helium for all models. In Tables 13–15 we show the LISM intensities of all nuclei species for all three models.

REFERENCES

- Ackermann, M., et al. 2012, *ApJ*, **750**, 3
- Adriani, O., Barbarino, G. C., Bazilevskaya, G. A., et al. 2011, *Sci*, **332**, 69
- Adriani, O., Barbarino, G. C., Bazilevskaya, G. A., et al. 2014, *ApJ*, **791**, 93
- Agostinelli, S., Allison, J., Amako, K., et al. 2003, *NIMPA*, **506**, 250
- Aguilar, M., Aisa, D., Alpat, B., et al. 2014b, *PhRvL*, **113**, 221102
- Aguilar, M., Aisa, D., Alvino, A., et al. 2014a, *PhRvL*, **113**, 121102
- Allison, J., Amako, K., Apostolakis, J., et al. 2006, *ITNS*, **53**, 270
- Berezinskii, V. S., Bulanov, S. V., Dogiel, V. A., & Ptuskin, V. S. 1990, *Astrophysics of Cosmic Rays*, ed. V. L. Ginzburg (Amsterdam: North-Holland)
- Bethe, H. 1933, *Handbuch der Physik*, Vol. 24 (Berlin: Springer)
- Burlaga, L. F., Florinski, V., & Ness, N. F. 2015, *ApJL*, **804**, L31
- Bzowski, M., Sokół, J. M., Tokumaru, M., et al. 2013, in *Solar Parameters for Modeling the Interplanetary Background*, ed. E. Quémérais, M. Snow, & R.-M. Bonnet (New York: Springer), 67
- Case, G. L., & Bhattacharya, D. 1998, *ApJ*, **504**, 761
- Cook, W. R., III 1981, PhD thesis, California Institute of Technology
- Cook, W. R., Stone, E. C., & Vogt, R. E. 1984, *ApJ*, **279**, 827
- Cummings, A. C., Stone, E. C., Lal, N., et al. 2015, ICRC, 318
- Duvernois, M. A., & Thayer, M. R. 1996, *ApJ*, **465**, 982
- Engelmann, J. J., Ferrando, P., Soutoul, A., Goret, P., & Juliusson, E. 1990, *A&A*, **233**, 96
- Fisk, L. A., & Gloeckler, G. 2012, *SSRv*, **173**, 433
- Fisk, L. A., & Gloeckler, G. 2014, *ApJ*, **789**, 41
- George, J. S., Lave, K. A., Wiedenbeck, M. E., et al. 2009, *ApJ*, **698**, 1666
- Glassgold, A. E., & Langer, W. D. 1974, *ApJ*, **193**, 73
- Gleeson, L. J., & Axford, W. I. 1968, *ApJ*, **154**, 1011
- Gloeckler, G., & Fisk, L. A. 2014, *GeoRL*, **41**, 5325
- Grenier, I. A., Black, J. H., & Strong, A. W. 2015, *ARA&A*, **53**, 199
- Guo, X., & Florinski, V. 2014, *ApJ*, **793**, 18
- Gurnett, D. A., Kurth, W. F., Burlaga, L. F., & Ness, N. F. 2013, *Sci*, **341**, 1489
- Gurnett, D. A., Kurth, W. S., Stone, E. C., et al. 2015, *ApJ*, **809**, 121
- Herbst, K., Heber, B., Kopp, A., Sternal, O., & Steinhiber, F. 2012, *ApJ*, **761**, 17
- Indriolo, N., Fields, B. D., & McCall, B. J. 2009, *ApJ*, **694**, 257
- Indriolo, N., Neufeld, D. A., Gerin, M., et al. 2015, *ApJ*, **800**, 40
- Ip, W.-H., & Axford, W. I. 1985, *A&A*, **149**, 7
- Iroshnikov, P. S. 1964, *SvA*, **7**, 566
- Jóhannesson, G., Ruiz de Austri, R., Vincent, A. C., et al. 2016, *ApJ*, **824**, 16
- Jokipii, J. R. 2001, in *The Outer Heliosphere: The Next Frontiers*, ed. K. Scherer et al. (Amsterdam: Pergamon Press), 513
- Kaganovich, I. D., Startsev, E. A., & Davidson, R. C. 2004, *PhPl*, **11**, 1229
- Kolmogorov, A. 1941, *DoSSR*, **30**, 301
- Kóta, J., & Jokipii, J. R. 2014, *ApJ*, **782**, 24
- Kraichnan, R. H. 1965, *PhFl*, **8**, 1385
- Krimigis, S. M., Decker, R. B., Roelof, E. C., et al. 2013, *Sci*, **341**, 144
- Langner, U. W., de Jager, O. C., & Potgieter, M. S. 2001, Proc. ICRC, **10**, 3992
- Lave, K. A., Wiedenbeck, M. E., Binns, W. R., et al. 2013, *ApJ*, **770**, 117
- Lodders, K., Palme, H., & Gail, H.-P. 2009, *LanB*, 712
- Lorimer, D. R., Faulkner, A. J., Lyne, A. G., et al. 2006, *MNRAS*, **372**, 777
- Lotz, W. 1967a, *ZPhy*, **206**, 205
- Lotz, W. 1967b, *ApJS*, **14**, 207
- Luo, X., Zhang, M., Potgieter, M., Feng, X., & Pogorelov, N. V. 2015, *ApJ*, **808**, 82
- McDonald, F. B. 1998, *SSRv*, **83**, 33
- Moskalenko, I. V., & Strong, A. W. 1998, *ApJ*, **493**, 694
- Moskalenko, I. V., Strong, A. W., Ormes, J. F., & Potgieter, M. S. 2002, *ApJ*, **565**, 280
- Moskalenko, I. V., Strong, A. W., & Porter, T. A. 2008, Proc ICRC (Merida), **2**, 129
- Potgieter, M. S., Vos, E. E., Munini, R., Boezio, M., & Di Felice, V. 2015, *ApJ*, **810**, 141
- Press, W. H., Teukolsky, S. A., Vetterling, W. T., & Flannery, B. P. 1992, *Numerical Recipes in FORTRAN, The Art of Scientific Computing* (New York: Cambridge Univ. Press)
- Ptuskin, V. S., Moskalenko, I. V., Jones, F. C., Strong, A. W., & Zirakashvili, V. N. 2006, *ApJ*, **642**, 902
- Scherer, K., Fichtner, H., Strauss, R. D., et al. 2011, *ApJ*, **735**, 128
- Seo, E. S., & Ptuskin, V. S. 1994, *ApJ*, **431**, 705
- Shikaze, Y., Haino, S., Abe, K., et al. 2007, *APh*, **28**, 154
- Spitzer, L., Jr., & Tomasko, M. G. 1968, *ApJ*, **152**, 971
- Stone, E. C., Cummings, A. C., McDonald, F. B., et al. 2013, *Sci*, **341**, 150
- Stone, E. C., Vogt, R. E., McDonald, F. B., et al. 1977, *SSRv*, **21**, 355
- Strauss, R. D., & Potgieter, M. S. 2014, *AdSpR*, **53**, 1015
- Strauss, R. D., Potgieter, M. S., Ferreira, S. E. S., Fichtner, H., & Scherer, K. 2013, *ApJL*, **765**, L18
- Strong, A. W., & Moskalenko, I. V. 1998, *ApJ*, **509**, 212
- Strong, A. W., Moskalenko, I. V., & Ptuskin, V. S. 2007, *ARNPS*, **57**, 285
- Strong, A. W., Orlando, E., & Jaffe, T. R. 2011, *A&A*, **534**, A54
- Taillet, R., & Maurin, D. 2003, *A&A*, **402**, 971
- Trotta, R., Jóhannesson, G., Moskalenko, I. V., et al. 2011, *ApJ*, **729**, 106
- Vladimirov, A. E., Digel, S. W., Jóhannesson, G., et al. 2011, *CoPhC*, **182**, 1156
- Webber, W. R. 1998, *ApJ*, **506**, 329
- Webber, W. R., & Higbie, P. R. 2008, *JGRA*, **113**, 11106
- Webber, W. R., & Higbie, P. R. 2009, *JGRA*, **114**, 2103
- Wiedenbeck, M. E. 2013, *SSRv*, **176**, 35
- Yoon, Y. S., Ahn, H. S., Allison, P. S., et al. 2011, *ApJ*, **728**, 122
- Zhang, M., Luo, X., & Pogorelov, N. 2015, *PhPl*, **22**, 091501